LRP 438/91 October 1991

DENSITY LIMIT DISRUPTION STUDIES IN THE TCA TOKAMAK

Z.A. Pietrzyk, A. Pochelon, R. Behn,
A. Bondeson, P.-A. Duperrex, B.P. Duval,
B. Joye, A.J. Knight, B. Marchal, C. Nieswand

Density Limit Disruption Studies in the TCA Tokamak

Z.A. Pietrzyk, A. Pochelon, R. Behn, A. Bondeson, P.-A. Duperrex, B.P. Duval,
B. Joye, A.J. Knight, B. Marchal, C. Nieswand

Centre de Recherches en Physique des Plasmas
Association Euratom-Confédération Suisse
Ecole Polytechnique Fédérale de Lausanne
21 av. des Bains, CH-1007 Lausanne Switzerland

Abstract

This paper describes density limit plasma disruptions that take place during the density increase in the plasma current flat top of TCA. In TCA, such disruptions have been observed to occur at two different densities, depending on discharge programming. An efficient method of achieving high density is to introduce a strong influx of neutral gas to the plasma, which was found to allow the plasma density to cross a range of densities that was otherwise unstable. In this kind of operation the disruption was observed to be approached from high to low plasma inductance in contrast to a slower density rise where the inductance is increasing. The study of the plasma temperature and density profiles as the disruption is approached, together with the characterisation of the mode and sawtooth activity, gives further insights into the physics of plasma disruptions.

1. Introduction

Plasma disruptions continue to be a problem in tokamak operation and present severe mechanical problems for the vessel and coils of a future reactor. Disruptions can quench the plasma in a very short time, producing large forces on the vacuum vessel and supporting structure which tend to occur at high plasma current, low safety factor and at high plasma density. This paper describes disruptions during high density operation in TCA.

The plasma may be terminated by the onset of a disruptive instability at the density limit, often called the Murakami limit [1]. The dependence of the density limit on the safety factor at the plasma edge, q_a, has been described by Hugill [2], and Greenwald *et al.* [3] produced a simple formula for the density limit which may be nearly universally applied. The fundamental dependence of this density limit is the safety factor, q_a although, different refuelling methods such as gas puffing or pellet injection can also influence the value of the density limit. In this paper we shall also show that the neutral particle flux during refuelling affects this limit.

A density limit disruption usually begins with a radiative cooling of the plasma edge and it has also been observed that the total radiated power approaches the ohmic input power just before disruption. Thus the total radiation was thought to play an important role in plasma disruptions [4]. Recent studies [5] have shown that disruptions depend more specifically on edge radiation profile rather than on the total radiated power. The cooling of the plasma edge squeezes the current profile so that the current gradient increases near the $q = 2$ surface, leading to increased mode activity, which corresponds to a distortion of the magnetic surfaces rotating with a velocity proportional to the diamagnetic drift velocity in the toroidal direction. As time progresses, the mode amplitude grows as its frequency decreases. Often in large machines, such as JET [6], the mode frequency becomes so low that the modes lock to the vessel and mechanical structure (the mode frequency goes to zero). The mode which leads to disruption is usually the $n = 1$, $m = 2$ and is located at the q=2 surface. The presence of this mode increases the energy losses from the plasma and in particular from the region between the q=2 surface and the plasma edge. Higher mode numbers also appear just before the disruption. Before the disruption, a strong increase in radiation from the region near the inner wall of the tokamak can be observed. This feature, which increases the inner edge radiation, is known as a Marfe and has been investigated theoretically [7]. The energy quench follows (in JET) after which the current (after a temporary increase) suddenly collapses, accompanied by a negative spike in the loop voltage, explained by a rapid redistribution of the plasma current and a corresponding reduction of the plasma inductance. The temperature generally falls more rapidly in large machines at the major disruption [6], after which, the current decays and the discharge terminates. Often this major disruption is preceded by a minor disruption, where the current drops only slightly and the plasma temporarily recovers. However, plasma disruptions do not always follow this JET example, especially when other machines or other types of operations are considered.

To reach the Greenwald density limit [3], the tokamak needs to be operated in such a way that the plasma discharge evolves stably. In TCA, the density limit encountered during quasi-static density operation (density and current are kept relatively constant by a feedback system) is generally about a factor of two lower than that predicted by the Greenwald limit which is probably due to the limited poloidal flux (volt-seconds) available on TCA. A strong influx of gas to the plasma chamber, which we call "hard puffing", permitted TCA to reach the Greenwald density limit and was used on TCA to reach high densities in a reproducible manner, within the available volt-seconds. It was also observed that near the Greenwald limit in TCA, the plasma β_t could reach a significant fraction of the Troyon β_t limit, using only OH heating.

We will present the results of a study concerning three different gas injection techniques. The achievable density in each scheme will be given and the different types of plasma disruptions encountered will be described. These three different gas injections regimes will be referred to as hard puffing, soft puffing and quasi-static density operation.

The density limit in hard puffing, soft and quasi-static operations can manifest itself either by a plasma current disruption terminating the discharge or by significant increase in the mode activity, which does not have a large effect on the plasma current, but inhibits a plasma density rise. It was difficult to predict which of these density limiting phenomena would actually occur during a given discharge, however, it was generally observed that at high values of q_a, the density was more likely to be limited by mode activity rather than by disruptions and in a very clean plasma, it is the mode activity that generally prevails over the disruptive limit.

The data presented in this paper was taken after boronisation [8] of the vacuum vessel wall. However, due to a slow degradation of the boron-carbride layer with time, the condition of the vessel wall evolved during the experiments. As several boronisations were applied to the vessel during these experiments, general trends on the density limiting phenomena during the wall degradation were also observed.

To understand the changes that the profiles undergo during various gas injections and on the way to disruptions, confinement analysis is largely used in this paper.

In Section 2 we describe the TCA tokamak, the specific diagnostics used in this experiment and the operating techniques which were used to produce high densities. In Section 3 we describe the hard puff discharges in detail, while Section 4 compares these discharges with other modes of operation during ohmic heating. Section 5 concentrates on the disruptions themselves and describes the different kinds of disruptions which occur in the various regimes. A physical interpretations of these observations will be presented in Section 6 and a summary of this paper is given in Section 7.

2. Experiment

(i) Machine and Diagnostics

The experiment was carried out in the TCA tokamak (major radius, $R = 61.5$ cm, minor radius, $a = 18$ cm, $B_\phi = 1.51$ T). Limiter discharges were produced at $q_a = 2.5$–6.5 in deuterium gas. The four carbon limiters were located in one poloidal plane. A description of the machine and the typical ohmic plasma conditions are given in [9].

The electron temperature and density profiles were measured by a ten point, single pulse Thomson scattering system. A ruby laser delivering 2–4 Joules was fired vertically into the Tokamak (Fig. 1). The ten point detection system was aligned in such a way that the entire minor radial profile below and up to r/a= 6/18 above the magnetic axis was observed. The scattered signal was collected by an *f*/1.6 lens and focused onto ten bundles of optical fibres, which conducted the light to separate polychromators [10]. The density was also measured at four radial positions by a four channel FIR interferometer operating at a wavelength of 447 μm, and with a single channel 2 mm microwave interferometer. The density profile was calculated from the Thomson scattering signal, preliminarily calibrated using Raman scattering from neutral hydrogen and the absolute calibration of the density profile was determined, on a shot to shot bases, from the line density measurements obtained with the interferometers.

The total radiated power was measured by a 16 channel bolometer [11,12]. The bolometer viewed the plasma horizontally, so that any "Marfe" activity, if present before a disruption, would be observed as an increase in the radiation measured by the central bolometer channels and thus unfortunately indistinguishable from an increase in radiation from the plasma centre.

As an additional electron temperature diagnostic, the soft x-ray absorber foil technique was used providing the central electron temperature throughout the discharge. A pair of diodes equipped with beryllium foil thicknesses of 275 and 625 μm, removes the most important impurity line emission; screening boron, carbon, oxygen and iron lines at the typical TCA electron temperatures. This system was calibrated against the Thomson scattering measurements and gave reliable results providing there were no runaway electrons present in the discharge.

A 15 diode horizontal soft x-ray camera was used to monitor the sawtooth activity.

An array of 8 magnetic probes located symmetrically around the torus in the toroidal direction was used to measure the θ-component of the oscillating magnetic field which allows measurements of n=0,1,2,3 modes. An additional non equally spaced array of up to 8 probes was used to determine the poloidal variation.

The plasma diamagnetism was also monitored, in order to determine the time dependence of the plasma inductance and to obtain the total plasma energy complemented Thomson scattering information. No assumptions about Z_{eff} or the ion temperature profile were necessary in this measurement.

In all the discharges studied, the plasma current was controlled by a feedback system. Although the plasma current was not perfectly constant for all discharges, none of the effects presented here are thought to be associated with changes in the current. Z_{eff} was maintained low (due to the repeated boronisation [8]) for the shots which are presented in this paper and just before disruption, Z_{eff} was estimated to be below 2 for low density shots and less than 1.3 for high density shots.

(ii) Operating Scenarios

For the disruption studies, TCA was operated in three different gas puff modes. These are hard puffing, soft puffing and quasi-stationary discharges [13]. Both soft and hard puffing discharges were obtained by programming a step function in the gas influx to the plasma chamber with the difference between soft and hard puffing only depending on the size of the step. The distinction between soft and hard puffing is best visible in the soft x-ray traces. For soft puffing, the soft x-ray signal is a monotonically increasing function of time during the density build up. In hard puffing, the soft x-ray emission passes through a maximum close to the beginning of the puff (Fig. 2a) which is associated with a marked maximum in T_e with very sharp increase in $\beta_p + l_i/2$ observed at approximately the same time.

Normalized jump of soft x-ray flux and $\beta_p + l_i/2$ are shown in Fig. 3. Soft puffing occurs for a particle flux input, $d\Phi_g < 3 \times 10^{17}$ part s^{-1}, with the plasma volume of 0.4 m^3, occupying 40% of the vessel volume. With particle fluxes greater than this value we are in the hard puffing regime. In a hard puffing discharge a moderate increase in the mode activity is observed, however, the mode amplitude saturates at a low level without leading to a plasma disruption (Fig. 2c).

A quasi-stationary discharge is one in which the line averaged density remains constant, after an initial rise, and is feedback controlled. The soft puffing discharge behaved in a similar way to a quasi-stationary discharge. The mode activity is markedly different between a hard puff discharge and the other two types of puffing. In particular, the frequency evolution and mode numbers are different. These observations will be discussed in detail in the following sections.

3. Hard Puff Discharges

The particular temporal behaviour of some of the discharge parameters in a hard puffing discharge is shown in Fig. 4 which shows the plasma current, loop voltage, line density, $\beta_p + l_i/2$, ion temperature and gas particle flux. The loop voltage goes through a local maximum at the beginning of the puff, at about $t = 90$ ms, then increases during the density rise. The maximum in the loop voltage, which occurs during a smooth density increase, can be explained by a corresponding increase in the plasma inductance manifested by a rapid increase of $\beta_p + l_i/2$ at approximately the same time shown in Fig. 4(c).

Figure 4(d) shows the time behaviour of the ion temperature measured using a neutral particle energy analyser. The ion temperature starts to increase shortly after the beginning of the hard puff, as the plasma density increases which can be accounted for by a decrease in the electron-ion equipartition time. The levelling off of T_i at later times is explained by a balance between the continuously decreasing equipartition time (the plasma density is still increasing) and the decreasing electron temperature.

Other parameters from the same series of discharges are shown in Fig. 5. A curious observation is that the electron temperature increases immediately after the start of the puff which was seen by both the continuous measurement obtained from the soft x-ray emission and from the Thomson scattering averaged over a series of similar shots. (The Thomson scattering data were taken in identical hard puffing shots with each experimental point being averaged over three to five shots. The error bars represent the standard deviation over those shots.)

The density profile measured by the Thomson scattering and the four channel interferometer flattens during the puff and later becomes more peaked (Fig. 5(b)) with the temperature profile peaked at the beginning of the puff Fig. 5(d). The plasma inductance was deduced from both the diamagnetic signal (solid line) and from the temperature and density profiles measured by Thomson scattering (circles). Assuming the plasma conductivity to be neoclassical [14], and the plasma inductance is given by,

$$l_i = \frac{2}{I_p^2} \int_0^a \frac{I^2(r)}{r}\, dr \qquad (1)$$

with

$$I_p(r) = 2\pi \int_0^r j(r)\, r\, dr \qquad (2)$$

where j(r) is the neoclassical current density profile and I_p is the total plasma current.

Temperature and density profiles at selected times during a series of reproducible hard puffing shots are shown in Figs. 6 and 7. The selected times correspond to the following features of the hard puffing shot: just before the gas puff ($t = 75$ ms); at the temperature maximum ($t = 89$ ms); at the time the density profile was flattest ($t = 100$ ms); and near the density maximum ($t = 165$ ms). The peaking and subsequent flattening of the temperature profile is very clear from these plots, in addition to the flattening of the density profile after the beginning of the puff, $t = 89$ and 100 ms.

The total electron energy can be calculated by integrating the electron pressure profile,

$$E_e = (2\pi)^2 R \int_0^a \frac{3}{2} n_e T_e\, r\, dr \qquad (3)$$

The total plasma energy contains the contributions from the electrons and the ions,

$$E_t = E_e + (2\pi)^2 R \int_0^a \frac{3}{2} n_e \frac{T_i}{Z_{eff}}\, r\, dr \qquad (4)$$

where it is assumed that the contribution from high Z ions to the total plasma energy is negligible. To evaluate the ion term an ion temperature profile must be measured or assumed.

The total plasma energy shown in Fig. 8(b), is calculated with the assumption that the ion and electron temperature profiles are identical and that the maximum of the ion temperature is that measured by the neutral particle velocity analyser. The ion energy calculated in this way is an underestimate, as measurements show in TCA [15] and other similar machines, that the ion temperature profile is broader than the electron temperature profile. As the ion temperature is lower than the electron temperature and Z_{eff} is not much larger than 1, the calculation of the total energy is not significantly influenced by errors in the ion temperature profile. We have assumed $Z_{eff} = 1.3$ for all hard puffing discharges. This is an average value calculated from the measured loop voltage over several shots using the neoclassical resistivity. The total energy in Fig. 8(b) shows, within the error bars, a monotonic increase with time which is attributed to the increasing line averaged density.

The toroidal beta, β_t, presented in Fig. 5(c) was calculated using the total plasma energy given by Eq. 4, shown in Fig. 8(b), where the experimental Thomson scattering profile were smoothed by polynomial fitting before integration. Using this data, a maximum in β_t and E_t was observed at about $t = 100$ ms, when the density profile was flattest. Figure 8(a) shows the total electron energy as a function of time calculated using Eq. 3, showing maximum also at about $t = 100$ ms.

The electron energy confinement time τ_{Ee} and the total energy confinement time τ_{Et} may be calculated from the following expressions with the assumption that the plasma is stationary,

$$\tau_{Ee,t} = \frac{E_{e,t}}{V_l I_p} \qquad (5)$$

where V_l is the loop voltage, I_p is the total current and $E_{e,t}$ is electron and total plasma energy. This underestimates the confinement time when the energy is increasing in time. Under our conditions, we estimate this error to about 10% on average but a more accurate calculation is not possible with the available diagnostics.

Fig. 8(c) shows the evolution of τ_{Ee} with time which shows a clear maximum. This maximum is a combination of two effects: the decrease in loop voltage (Fig.4a) and the increase in the electron energy. These two factors in Eq. 5 contribute to a relatively large increase in τ_{Ee} at about 100 ms. It is this increase in τ_{Ee} that leads to an increase in the electron temperature at the beginning of the hard puffing. This is a demonstration that the energy confinement time can improve for ohmically heated plasmas with a flat density profile, similar to that of an H-mode neutral beam heated discharge, but not necessarily for the same physical reason.

The total energy confinement time shown in Fig. 8(d) also exhibits a small local maximum, although this maximum is nearly within the error bars of the measurements. The values of τ_{Et} measured using the plasma diamagnetism are within the error bars of those calculated from Thomson scattering although there are indications that our diamagnetic measurement somewhat underestimates the total plasma energy. From these two measurements, scattering and diamagnetism, either τ_{Et} saturates after $t \approx 100$ ms, or starts to decrease with the line averaged density reaching about 5×10^{13} cm^{-3} at this time.

To investigate the cause of improved confinement during the beginning of hard puffing, we examined the magnetic broad band fluctuations near the plasma edge. The signal was monitored using a b_θ magnetic probe and the amplitude was recorded after electronic band-pass filtering at several different frequencies, covering the range 50–560 kHz. After the start of the puff, the amplitude of the higher frequency components was observed to decrease rapidly. A possible explanation is that the high frequency oscillations are connected with ∇p or ∇T driven microturbulence which are reduced at the plasma edge after the gas injection as these gradients diminish. Figure 9 shows two fluctuation spectra, just before and just after the start of the puff. While the amplitude of the low frequency oscillations remains constant, the high frequency components seem to drop over a factor of five. As these oscillations are related to plasma edge turbulence [16], then this reduction could also lead to an improved energy confinement at the edge. However, the amplitude of the Mirnov oscillations starts to increase at the same time (Fig. 10), which may be a reason for degradation of the energy confinement at later times. However, the maximum in τ_{Et} occurred when the Mirnov oscillations had already saturated.

For shots made many shots after boronisation of the vacuum vessel (more than 500 shots) and under soft puffing conditions, the total radiated power reaches the ohmic input power when the density reaches the soft puffing disruption limit ($n_e = (4–5) \times 10^{13}$ cm^{-3} at $q_a = 3.2$). Under hard puffing operation, the total radiated power closely follows the ohmic power up to the (higher) density limit (Fig. 11). This would suggest that the soft puffing disruption is associated with the radiation and that hard puffing prevents this disruption by proper gas influx programming. This explanation, however, is not supported by the fact that in clean discharges, made shortly after a boronisation, the radiated power is much less than the ohmic power at the soft puffing limit and reaches the ohmic power only very close to the hard puffing density limit (Fig. 12). We must conclude, then, that the total radiated power is not a determining factor affecting the onset of a disruption in boronized TCA discharges. The time history of the radiation profiles for pure and impure plasmas are similar, an initially hollow radiation profile which fills near the hard puff density limit. The edge radiation may be important in both cases.

4. Comparison with Soft Puffing Discharges

In Fig. 13 we show the profiles of electron temperature, density and pressure during hard and soft puffing discharges before disruption. In each case, the data are averaged over four identical shots and normalized to their maximum values. Best fit sixth order symmetric polynomials to the data are also shown, where the points represent the mean values and the error bars indicate the standard deviation of the measurements. Only the density profile, shows a clear distinction, being broader for soft puffing, so the ratio of the edge to the central density is high near the soft puffing disruption limit where it is low near the density limit for hard puffing. The absolute value of the density however, was higher across the minor radius for the hard puff shots, except the density between the plasma edge and q=2 surface, where shot to shot variations combined with the accuracy of our measurements do not permit us to draw any definite conclusions. Thus, the onset of a disruption may be associated with the edge density or the density at the q=2 surface. The pressure and temperature profiles appear to be slightly broader during hard puffing, but the difference is within the error bars and there is no significant difference between these profiles before disruption for soft and hard puffing. It is interesting to note that all the temperature profiles normalised to the temperature at the q=1 surface show profile consistency similar to observation in ASDEX[17] and other tokamaks.

The total electron and total plasma energies, calculated according to Eqs. 3 and 4, are plotted against the line averaged electron density in Fig. 14 where the lines in the figure are drawn to guide the eye. In quasi static operation the total plasma energy varies approximately linearly with line density over the explored density range, with hard puffing however, higher values of energy are measured for low densities, and at higher densities the plasma energy returns to the line extrapolated from the soft puffing data. The electron energy is also higher at low density for hard puffing, but falls slightly below the extrapolated soft puffing line at high density, which indicates that the electron energy confinement is slightly improved for low density and degraded for high density with respect to the linear dependence. At this point it should be mentioned that the data presented in Fig.14 and Fig. 15 were taken during a density rise only and therefore one cannot be certain from the data that this is only a density dependence.

The effect of improved energy confinement shown in Fig. 14 as changes in energy versus density can be seen in Fig. 15, where the corresponding confinement times τ_{Ee} and τ_{Et}, have been plotted. The electron energy confinement times are similar for soft and hard puffing at low densities. At higher densities, above the disruption limit for soft puffing, τ_{Ee} deteriorates so that the high density data fall beneath the soft puffing data. In the lower plot the value of τ_{Et} calculated from the plasma diamagnetic loop signal is shown for one particular hard puffing shot. To check the consistency of the data, τ_{Et} was also calculated from the measured $\beta p + l_i/2$ signal and l_i calculated from the measured temperature profile (Eq. 1) assuming a neoclassical resistivity. The value of βp was used to compute the total plasma energy, thus leading to an estimate of τ_{Et}. (shown as triangle in the Fig. 15). This calculation does not require any assumption about the T_i profile or the value of Z_{eff}, but assumes a neoclassical conductivity. The values of τ_{Et} calculated in this way are consistent with those calculated by integration of the energy density profiles (equations 4 and 5) and with those calculated from the diamagnetic signal.

The Hugill density limit in TCA can be calculated using the following expression, given in Greenwald [3],

$$n_e = k\, I_{ave} \quad [\mathrm{m}^{-3}] \qquad (6)$$

where k is the plasma elongation and I_{ave} is the average plasma current in MA. In the cylindrical approximation, this can be written,

$$n_e = \frac{5\, B_\phi}{\pi\, \mathrm{R}\, q_a} \qquad (7)$$

which for the TCA tokamak becomes,

$$n_e = \frac{2.61 B_\phi}{q_a} \quad [\mathrm{T}, 10^{20}\, \mathrm{m}^{-3}] \qquad (8)$$

The Troyon toroidal beta limit, β_{Troyon}, can be calculated from the following expression [18],

$$\beta_{Troyon} = \frac{2.2\, \mu_0 I_p\, a}{B_\phi} \quad [\%] \qquad (9)$$

for TCA we can write simply $\beta_{Troyon} = \frac{4}{q_a}$.

To examine how close the hard puffing shots approached these two limits, we show in Fig. 16 the inverse safety factor plotted against the line averaged density and plasma β_t. In this figure, shots where the density is limited by a disruption (triangle) and mode activity (square) are shown and we see that for some shots the density reached the Hugill/Greenwald limit. In the same shots, the plasma β_t achieved only a fraction of the Troyon limit, suggesting that it is the density barrier which primarily limits the plasma parameters in these discharges, although the rather high β_t value might have an effect on the way in which the plasma eventually disrupts. We emphasize that using the hard puffing technique, ~ 60% of the Troyon β_t limit was achieved in purely ohmically heated plasmas. The soft puffing method gave less than half this value. These densities were obtained only transiently at the end of the discharges, due to the volt-seconds limitation and it was not possible to investigate whether a steady state condition could be reached just below the hard puffing density limit.

5. Disruptions

Depending on the parameter regimes, different paths to disruption have been observed. The main differences were observed between shots with $q_a < 3$ and those with $q_a > 3$, and with either hard or quasi-static/soft puffing operation. Throughout this paper we have used the cylindrical q_a, the toroidal q_ψ being approximately 13% higher [19]. We will describe in detail the disruptions which occurred in each of these main categories.

Disruptions at $q_a < 3$

In the shots examined in this low q_a regime, we did not observe any differences in the disruptions for hard and soft puffing. To obtain discharges with this low edge q value, we used a low plasma density to cross q=3 without disruption during the initial fast current rise. The density could be increased after reaching approximately $q_a = 2.6$, when the mode burst related to q_a =3 crossing had vanished. The first sign of an imminent disruption, during the current flat top, is a growth in the magnetic mode activity (Fig. 17). At a disruption, the plasma current after initially increasing slightly, decreases rapidly i.e. the rate of change of current started at about -20 MA s^{-1}, and increased to, -120 MA s^{-1}, at the point where the current reached a value corresponding to $q_a = 3$, when the plasma becomes even more unstable. The loop voltage shows a large negative spike at the beginning of the small current rise, indicating a sudden redistribution of the plasma current. In Fig. 18 we show the electron temperature and density profiles measured in the same shot, 4 ms before the disruption. No visible degradation in the plasma energy can be observed at this time, even though the mode activity is high. The "energy quench" [7] may still have been present, but after the Thomson profile measurement and closer to the disruption (less than 4 ms). The toroidal β_t remains at ~ 60% of the Troyon limit for these shots, as for $q_a > 3$, even through density is only about half the Greenwald limit, (see Fig. 16). This suggests that in this regime, the β_t limiting phenomena play a more important role than the density limiting phenomena.

Disruptions at $q_a > 3$

Above $q_a = 3$ the hard puffing discharges were very reproducible and we were able to directly compare data from different shots. With $q_a > 3$ differences were observed between the soft and hard puffing disruptions with disruptions of either type occuring only for $q_a < 4.5$. At higher values of q_a, the density was limited by mode activity and, with boronised walls, no disruption took place.

Figure 19 shows the plasma current and loop voltage for soft and hard puffing disruptions. The behaviour of the loop voltage is quite different from the case with $q_a < 3$ and in particular for the soft puff where the loop voltage displayed a positive spike before the current started to decrease. In this particular shot, there was no large negative spike, which was sometimes observed 5–7 ms later, when the current had already decreased to about half of the plateau value. The lack of a negative spike would indicate that there is no rapid broadening of the plasma current profile during the disruption, but that the current is eroded from the edge. The initial rate of current decay is –18 MA s^{-1} and subsequently decreases (i.e. the current decay is more or less exponential) in a manner similar to that observed in JET [7]. The hard puffing disruption again begins with a negative loop voltage spike, but which is not as high as for $q_a < 3$.

Temperature profiles near a hard puff disruption are shown in Fig. 20. These data were taken at $t = -15$ ms (before) and at $t = 5$ and 8 ms (after the disruption). In this set of data the temperature on axis at $t = 5$ ms is the same as before disruption, $t = -15$ ms, but the profile is highly peaked. Although these profiles were measured from different shots, it is clear that the temperature on axis remains high, for at least some of the discharges. This is also observed for a soft puff disruption, as can be seen in Fig. 21, where the electron temperature obtained from the soft X-ray emission is shown as a function of time, together with the temperature (one time point) measured using Thomson scattering. The drop in temperature from 600 to 400 eV may be associated with the energy quench. The small drop in the temperature in TCA clearly differs from the large temperature drop to 10 eV in JET [7] (estimated from the current decay and supported by other measurements at the beginning of disruptions), and also differs from the fast drop to 150 eV observed in TFR [20]. This suggests that the fall in temperature is more significant for larger machines. A possible explanation for this is that in smaller machines, the ratio of the sensitive time scales to the time for conduction along stochastic field lines is smaller and that as a consequence a temporary loss of confinement during disruption does not lead to the immediate loss of plasma [21].

The differences in the level of magnetic mode activity for soft and hard puffing has already been mentioned (Fig. 2). In Fig. 22 we show plots of the mode frequency versus time for soft and hard puffing disruptions. In brackets are the m,n mode numbers associated with oscillations measured at various frequencies. The disruption itself can be identified in both cases by a broadband feature, occurring at $t = 132$ and 170 ms, respectively. For the lower graph, the hard puff starts at 75 ms, leading about 10 ms later to mode amplitude and frequency increases, with the frequency stabilizing at about 17 kHz. This mode frequency is about 25% higher than that associated with soft puffing. The amplitudes of the harmonics in the soft puffing discharge are much higher and the peaks are narrower than in the hard puffing shot. The mode frequency decreases with time for the soft puffing discharge which becomes more rapid as the disruption is approached. The decrease in mode frequency starts when the mode amplitude becomes large. Before the hard puffing disruption, the mode frequency begins to decrease, (but not as much as in soft puffing) and then, less than a millisecond before disruption, the mode frequency rapidly increases (Fig. 23). The latter effect is not visible in Fig. 22 due to the large (4 ms) window needed for Fourier analysis.

Another difference between soft and hard puffing is the appearance of multiple frequency oscillations during hard puffing. This can be seen in Figs. 24 and 25, where a frequency spectrum and raw data from a poloidal probe are shown. The relative amplitude of the modes for soft and hard puffing can be compared using Fig. 24. and the apparent beating of two or more frequencies in Fig. 25 could be the result of oscillating magnetic islands due to the velocity shear [22].

Tables I and II show the mode numbers calculated from a Fourier analysis of the magnetic probe signals for hard and soft puffing, respectively. The poloidal m numbers were calculated taking into account toroidal corrections and plasma shift [23]. The magnetic signals show that a low amplitude (*m*,*n*) = (2,1) mode is present early in the discharge for both hard and soft puffing. Later, modes with (*m*,*n*) = (3,2) and (5,2) appear in some cases although, just before disruption, the (2,1) mode always dominates. For hard puffing there are some uncertainties in the determination of modes for times later than about 120 ms, when the mode activity has a very broad spectrum. The low frequency of this broad band spectrum (about 10 kHz) shows a good fit to both (1,1) and (3,1) modes. Since it is not likely that one would see an effect from the q=1 surface, one would rather expect this mode to be (3,1), but it has a lower frequency than the (2,1) mode which dominates at this time. If indeed this low frequency oscillation is the (3,1) mode, then it would indicate a lower pressure gradient at q=3 than at the q=2 surface. However, it is possible, but not extremely likely, that the (1,1) mode is originating from the plasma edge rather than from the q=1 surface. Finally, possibility of (1,1) helical perturbation and existence of (1,1) island is reported TFR [20] group.

The comparison between the amplitude of mode oscillations during soft and hard puffing shown in Fig. 26 is interesting. The hard puffing discharge modes saturate at low amplitude and grow rapidly just before disruption. For soft puffing the modes grow, remain almost constant for several milliseconds, and then finally grow again, leading to the plasma disruption. The modes in the soft puffing discharge, during the time when they remain at a large constant amplitude, are about an order of magnitude higher than in the hard puffing discharge. At the same time the mode frequency goes down. In fact, the mode frequency begins to slow down only when the mode amplitude becomes high.

The toroidal and poloidal ion rotation velocities were measured at $r/a \approx 11/18$ using the Doppler shift of a Carbon V spectral line and at the edge using a Carbon III line [24]. These measurements indicate that, in general, the ions rotated with a velocity of about 2×10^3 ms^{-1}, an order of magnitude smaller than the velocity of the magnetic modes in toroidal direction. During hard puffing the toroidal velocity of the ions approaches zero at the edge, or even reverses (Fig. 27), while the velocity of the modes and poloidal ion velocity increases. Changes in velocity can be explained by changes in the radial electric field [24,25] and would indicate an increase in the electric field during hard gas puffing to the plasma. This may have some influence on the confinement and through velocity shear on the stabilisation of modes in the plasma.

The current density profile is also different in hard and soft puffing. Here, as an illustrative example, we show sawtooth activity for soft and hard puffing (Fig. 28). For $q_a > 4.5$, the sawtooth activity disappears for soft puffing discharges. The sawteeth appear again for hard puffing just after the start of the puff. More evidence of current peaking for hard puffing discharges at lower q_a. will be shown later.

6. Physical Interpretations

(i) Temperature Increase during Hard Puffing Discharges

The increase in electron temperature at the beginning of strong puffing was surprising. We have observed that the strong input of gas causes a flattening of the density profile, $dn/dr \approx 0$ over large fraction of the plasma cross section, together with a rapid increase in density. There is a strong density gradient at the plasma edge, and a very flat density profile inside the plasma with a peaked temperature profile at the same time. It appears that the increase in electron temperature is caused by a reduction in the plasma edge losses due to conduction or convection. The reduction of losses from the plasma edge may be linked with the observed high frequency magnetic turbulence reduction during hard puffing. This high frequency turbulence correlates inversely [26] with energy confinement time, which supports the measured increase in the electron energy confinement time during initial part of the hard puffing. The mechanism of this loss reduction could be the reduction of the density fluctuation, if the magnetic oscillations are correlated with density fluctuations and the reduction of density fluctuations could be related to a decrease in microturbulence driven by ∇p or ∇T, which are reduced by the influx of the cold gas. One should also mention the reduction in toroidal and increase in poloidal velocity (Fig. 27) at this time indicating increase negative electric field which may also influence the loss reduction. It is interesting to note that similar changes in rotational velocity were observed in DIII-D during L-H transition [27]

(ii) Stabilization of Low Density Disruptions

Mode analysis of soft puffing shots indicates that the instability grows at the $q = 2$ surface. Initially, only modes with $(m,n) = (2,1)$ are present, followed later by (4,2) and (6,3) modes before disruption. Resistive MHD theory [28,29] suggests that a mode is stable only if $\Delta' < 0$, where,

$$\Delta' \equiv \lim_{\delta \to 0} \frac{1}{\Psi(r_s)} \left[\frac{d\Psi}{dr}(r_s + \delta) - \frac{d\Psi}{dr}(r_s - \delta) \right] \qquad (10)$$

Here, $\Psi = rB_r$ and r_s is the radius of the resonant surface. This definition is not very useful if Δ' is to be calculated from experimental profiles since a precise value of the current density derivative is required. The current density could be calculated from the measured temperature and density profiles with the assumption of neoclassical conductivity, but the data would have to be interpolated in some fashion to obtain the gradient. As the result would be strongly dependent on the fitting procedure used, no attempt was made in this direction. One can, however, examine equation (10) to ascertain what changes in the profile could make the plasma more or less stable at a given surface. Following [29], we say that a current gradient, $dj/dr < 0$, is destabilizing at a rational surface if it occurs inside the given surface and stabilizing when it occurs outside. A stable situation can still exist, if the current gradient is well inside the rational surface.

At the start of a hard puff, the current density profile becomes more peaked, as observed from the scattering profiles, diamagnetic measurements and confirmed by the soft x-ray diagnostic. This may be associated with a reduction of the edge temperature. The current profile, if pushed far inside the $q = 2$ surface, becomes more peaked and prevents the growth of the $m = 2$ mode which would otherwise lead to a disruption during soft puffing. However, the equilibrium must cross an unstable profile region with a high gradient near the $q = 2$ surface. This must be done quickly in order to minimize effects of instability. We believe that this is why hard puffing works whereas soft puffing does not. This scenario is only partially supported by the data. Indeed, the plasma inductance goes through a maximum at the start of a hard puff (Fig. 5d), which is higher than its value before the soft puffing disruption. Then, the inductance decreases steadily until the plasma disrupts, which is in agreement with this explanation. However, although the current density profile (Fig. 29), calculated from the temperature and density profiles changes at the beginning of the hard puff, it remains almost unchanged in the vicinity of the $q = 2$ surface ($r = 14$ cm). This may be due to the limited accuracy of our measurements since if our Δ' explanation is correct, there should be a change in the current gradient near the $q = 2$ surface. The determination of the current profile from the measured plasma temperature and density is questionable as it depends strongly on how the experimental data are smoothed.

In quasi-static density operation, despite keeping the current and the density under feedback control, the plasma profiles have not fully reached steady state and the plasma inductance typically slowly increases with time (current is diffusing into the plasma). Parasitic signals in the diamagnetic measurements do not allow us to determine the inductance increase precisely in case of soft puffing or quasi-static density operation. The current density profile may become more peaked, at later time, either by slow current diffusion into the centre, or by cooling of the plasma edge by radiation which increases the current density gradient near the q=2 surface. When the current gradient at $q = 2$ rises above a certain threshold, the mode activity increases and the frequency is reduced by a flattening of the pressure profile dropping from 13 to 6 kHz just before disruption.

At the beginning of a hard puff, the pressure profile near the $q = 2$ surface becomes very steep, which increases the diamagnetic drift velocity and corresponds to the observation of increased mode frequency. The magnetic signal shows a beating of different mode frequencies Fig. 24 and Fig. 25. This may be correlated to oscillations of q=2 island size induced by shear in the poloidal flow [22]. These oscillations do not always correlate with the sawtooth period.

(iii) High Density Disruption

Prior to the hard puffing density limit, the temperature and pressure profiles are almost identical to those measured before a soft puffing disruption or a disruption during a quasi-static operation, although the density is practically double. The only significant difference with soft puffing is a local flattening of the pressure profile near the $q = 2$ surface (Fig. 13), which results in the lower mode frequency observed. The lower mode frequency observed in soft puffing and quasi-stationary discharges compared to hard puffing discharges is consistent with the relative flatness of their pressure profiles, since the diamagnetic drift velocity depends on the pressure gradient. For hard puffing, there is a dramatic increase in the mode frequency one to three millisecond before the disruption (Fig. 23) in many of the shots which corresponds to steepening of pressure gradient at this time near q=2 surface.

In hard puffing, the inductance quickly increases at the start of the puff and crosses through the presumably unstable region in soft puffing. It increases so rapidly that the modes do not have sufficient time to grow to a high amplitude. At this time strong current modification occurs. Then, the inductance starts to decrease (Fig. 5d), so at later times, the unstable region is approached with a decreasing plasma inductance, the current profile broadens again producing a large current gradient at the $q = 2$ surface. Soft and hard puffing shots show the presence of $(m,n) = (2,1)$ modes. A (4,2) mode appears before the disruption for hard puffing, but its amplitude is much smaller than those of the higher order modes observed with soft puffing (Fig. 22 & 24). The difference in harmonic amplitude is presumably related to the fundamental mode amplitude, which is considerably larger for soft than for hard puffing.

Additional evidence of the approach to the instability region from high to low inductance, for high puff operation comes from the behaviour of the sawtooth activity. The sawtooth activity before a hard puff disruption is shown in Fig. 30. For t<150 ms the q=1 surface is at r≈5.3 cm, but at t=150 ms inverted sawteeth start to appear at this radius which indicates a reduction of the q=1 radius. As the total plasma current is constant and assuming a constant current density inside the q=1 surface, this shrinking of the q=1 surface would give rise to an increased current outside the q=1 surface, reducing the inductance and triggering the instability at the q=2 surface. The first sign of the disruption is the large spike in the soft x-ray intensity, near the q=2 surface at t≈173.5 ms. This disturbance appears between the q=1 and q=2 surfaces (Fig. 30) and sometimes propagates inward from the q=2 surface. Following this, (by a little more than a millisecond), a drop in the x-ray emission propagates in both directions from the q=1 surface and the plasma disrupts. Sometimes, the disruption is minor and a further major disruption occurs starting at the q=1 surface and propagating outwards. The low density limit (soft puffing) disruption shows similar x-rays features, with an increasing plasma internal inductance, indicating an approach to the unstable region from below. It should be noted that the decrease of the soft x-ray signals is not associated with a complete collapse of the central electron temperature (Fig. 20) but rather with a reduction of the total plasma energy.

The approach to the instability with decreasing plasma inductance in the case of hard puffing discharge is a significant difference in the disruption mechanism. We have attempted to experimentally verify whether the initiation of a hard puffing disruption was linked to a broadening of the current profile, by trying to postpone the disruption using a second hard puff. The second puff was programmed at 140 ms in target discharges with reproducible minor disruptions at 160 ms. The second puff postponed the disruption by 15 ms during which time the line average plasma density increased by a further 25%. This experiment confirms that the approach to the unstable region in hard puffing operation is in fact from a peaked to a broadened current profile. In terms of tokamak operation using two hard puffs, however, was not a convenient way to produce reproducible high density plasmas on a shot to shot basis, since the large amount of gas released at the end of the discharge produced uncontrolable recycling in several following discharges.

The plot of l_i versus $q_{a,}$ in Fig. 31 shows qualitatively what occurs during a hard puffing discharge. In this figure, the upper limit of the lower stable region of operation is plotted from a collection of soft puff shots and the upper limit of the upper stable zone shows the maximum possible l_i for given a $q_{a,}$, obtained by assuming that all the plasma current is inside the $q=1$ surface and that q is unity everywhere inside this surface. In hard puffing discharges, the inductance clearly rises above the lower stable limit and reaches almost the maximum possible value (Fig. 5d) before subsequently decreasing, i.e. it crosses the stability boundary. Since the plasma is obviously stable with this higher value of inductance, there must be another stable region above this boundary. The boundary of this second stable region is only drawn schematically, as it was not investigated over a broad range of q_a. However, the unstable region is rather narrow for q_a=3.2, as the profiles near the instability from soft and hard puffing are very close. For q_a<3 a second stable region was not observed using hard puffing operation. For large $q_{a,}$ this second stable region is not very well documented, as we do not have a second diagnostic - as sawteeth disappears - with which to verify if the inductance goes down with time as indicated by the diamagnetic loop. However, at q_a=3.2, the l_i diamagnetic measurements was confirmed by Thomson scattering temperature profiles and changes in the inversion radius from the sawtooth activity.

For $q_a > 3$ the density can be limited either by disruption or by increased mode activity. For $q_a \geq 4.5$, the density is always limited by mode activity, but without a plasma current disruption. In such cases the mode frequency also initially decreases indicating a flattening of the pressure profile near a rational surface. Later, the mode frequency again increases and the plasma returns to its state before the mode started to grow (Fig. 32). The presence of large modes increases particle and energy losses from the plasma edge which presumably produces more peaked current profiles, (we do not have time depend profile studies for these discharges) a situation which resembles hard puffing for $q_a = 3.2$, but without the density increase. For $q_a \geq 4.5$, the modes start with $(m,n) = (3,1)$, indicating an oscillation at the $q = 3$ surface and then the mode is stabilized by the hard puffing and its amplitude is reduced (Fig. 32). A little later, a (2,1) mode starts to grow with a lower frequency so the change of the mode is visible in Fig. 32 as a sudden drop in frequency at 90 ms. This mode grows until it is strong enough to expel particles from the plasma, preventing a further increase in the density (Fig. 32). This reduces the plasma pressure outside the $q = 2$ surface, increasing the pressure gradient at that surface, which in turn increases the diamagnetic drift velocity and gradually increases the mode frequency . At the minimum frequency a spike is observed on soft x-ray traces occuring between the q=1 and q=2 surfaces, as in a disruptive plasma and propagates through the plasma without disrupting the current.

Qualitatively, these results do not strongly depend on the purity of the plasma. The hard puffing density limit is slightly higher (about 20%) in clean plasmas and disruptions are statistically slightly less prone to occur. In these clean plasmas, just after boronisation, the density is also more likely to be limited by modes rather than by a disruption. The total radiated power reaches the ohmic heating input power at the soft puffing density limit in dirty plasmas, whereas in clean plasmas it is less than half the ohmic heating power. However, this large changes in the radiation level only slightly alters the maximum achievable density and does not change the mode behaviour before disruption. The total radiation is therefore not a good indicator of the possible onset of a disruption.

At the hard puffing density limit, the radiative losses are equal to the ohmic input power and the radiation profile is peaked. However, for less pure plasmas the total radiated power reaches the ohmic power at the (lower) soft puffing density limit. Hollow radiation profiles at high density and with dirty plasmas suggest that the increased radiation is from low Z ions which predominantly increase the radiation near the plasma edge.

The toroidal β reached is ~ 60% of β_{Troyon} at the hard puffing density limit with only ohmic heating.

(iv) Plasma Resistance during Current Disruption.

To understand why the current decays so quickly during disruption one can estimate plasma resistance during this process by considering the plasma as an electrical circuit with only resistance and inductance terms. We neglect the influx of energy from the transformer, as the power delivered to the plasma from the transformer is small in comparison with the power dissipated during the current disruption. The circuit equation can be written:

$$\frac{d}{dt}(L_{eff} I) + R_{\Omega} I = 0 , \qquad (11)$$

where $L_{eff} = L_i + L_{ex}$ is the total circuit inductance, R_{Ω} is the plasma resistance, where $L_i = 0.5\mu_0 R l_i$ is the plasma internal inductance and $L_{ex} = \mu_0 R[\ln(\frac{8R}{a}) -2]$ is the inductance outside of the plasma.

On can rewrite this equation as,

$$L_{eff}\frac{dI}{dt} + (R_{\Omega}+\frac{dL_{eff}}{dt})\, I=0, \qquad (12)$$

where the expression in the brackets is called the effective plasma resistivity $(R_{\Omega}+ \frac{dL_{eff}}{dt}) = R_{eff}$. If R_{eff} is constant in time this gives an exponential decay for the current

$$I = I_0 \exp(- \frac{t}{t_0}) ,$$

where $t_0 = \frac{L_{eff}}{R_{eff}}$ is the current decay time, for $\frac{dL_{eff}}{dt} = 0$;

R_Ω can be calculated from measured t_o and l_i with the assumption [7,20] of $\frac{dL_{eff}}{dt} = 0$; However, l_i can be measured only before a disruption and the assumption $\frac{dL_{eff}}{dt} = 0$ during a disruption is not strictly correct.

Nevertheless, for TCA plasmas with $q = 3.2$, we have $l_i = 1.5$ which gives $L_i = 5.76\ 10^{-7}$ H and $L_{eff} = 1.5\ 10^{-6}$ H, so with a typical $t_o = 12$ ms, we obtain $R_\Omega = 1.3\ 10^{-4}\ \Omega$. This is 6 times larger than the R_Ω before disruption calculated from the plasma current and the loop voltage. Calculating $<T_e>$ from this resistivity gives $<T_e> = 50$ eV while the measured Thomson scattering profile after disruption gives $<T_e> = 100$ eV, a difference that was observed from several Thomson scattering profiles after the disruption where $<T_e>$ has a factor 2 to 3 higher than that calculated from plasma resistance. The resistivity calculated this way always underestimates the volume averaged temperature if classical resistivity and constant Z_{eff}, is assumed. However, the assumption of classical resistivity is questionable during disruption due to strong turbulence[30].

For q=2.4, the current decay time $t_o = 1$ ms is much shorter, yielding $R_\Omega = 1.5\ 10^{-3}\ \Omega$ which is more than 100 times higher than R_Ω before the disruption. Assuming classical conductivity, the increase in the plasma resistivity would require a factor of 20 reduction in the average plasma temperature. This would bring the average plasma temperature into the 10 eV range. Due to the rapid decrease of current for q<3 we do not have any Thomson scattering data after disruption for this parameter range. The soft x-ray temperature does not show a large temperature decrease at the disruption, but this diagnostic is not reliable for a rapidly changing signal, due to a possible impurity influx or increased runaway electron population which occurs at this time.

7. Summary and Conclusions

Disruptions behave differently depending on the operational parameters of the machine. In TCA, a quantitative distinction in disruption behaviour can be drawn according to the value of q_a. Quantitatively, disruptions behave differently for $q_a<3$, $q_a \approx 3.2$ and $q_a>4$. Most of the data in this paper was taken with $q_a \approx 3.2$. We start by summarising disruptions under these conditions.

Scenario before disruption for $q_a \approx 3.2$:

Soft puffing - plasma inductance increases monotonically

Hard puffing - plasma inductance initially rises and then decreases.

- *Disruption precursor:*

Different for soft and hard puffing.

1. Soft puffing:

A large perturbation at the q = 2 surface. Near the disruption, a (2,1) mode and associated higher harmonics (4,2) and (6,3) are observed with very well defined frequencies. The total radiation from a clean plasma is much smaller than the ohmic input power and only reaches this level for an impure plasma.

2. Hard puffing:

The plasma inductance increases rapidly at the beginning of the puff, quickly crossing the unstable region. At this time the (m,n) = (2,1) mode grows and its frequency increases. The (3,2) and (4,2) modes are also observed, but at a very low level. Before disruption, the amplitude of the (2,1) mode is much smaller than for soft puffing and is not accompanied by a large level of higher harmonics and just before disruption (one to three milliseconds) the mode accelerates for many of the shots. The disruption is preceded by broadening of the mode spectrum, rather than by an increasing mode amplitude and the (3,1), (3,2), and (5,2) modes are than observed. At the time of the plasma current collapse there is a negative loop voltage spike and for a clean plasma, the radiation power reaches the ohmic power level at the time of disruption.

- *Collapse phase of disruption.*

This phase is similar in both soft and hard puffing cases, except for the first loop voltage spike, which is positive for soft and negative for hard puffing disruptions. The pressure, temperature and current profiles just before the disruption are very similar in both cases. The first sign of a disruption appears between the q=1 and q=2 surfaces, with the strongest disturbance at the q=2 surface. The q=1 region is then destabilized and the current disrupts with the final level of mode activity similar in both cases. The temperature profile during the current collapse is very peaked, with little change in the on axis electron temperature, but a strong decrease at the edge. For this value of the q_a the plasma density was either limited by a disruption or by mode activity.

- *Physical interpretation:*

1. Soft puffing - large modes on q=2 the surface destroy the confinement in the outer region of the plasma.

2. Hard puffing - precursor involves several modes with a broad spectrum first inside and on the q=2 surface, then later outside this surface.

Disruption for q_a<3.

The region, $q_a \approx 2.5$ was investigated. There is no difference between soft and hard puffing for this q_a. The disruption proceeds very rapidly for this value of q_a with the current decay 10 times faster than for q_a≈3.2. This is most probably explained by immediately reaching the unstable q_a=3 when the current decreases. The resistivity calculated from the current decay is very large, indicating either a very low temperature or a strongly nonclassical resistivity. For this low qa value the density was always limited by a disruption.

Density limit for $q_a>4$.

Here, discharges at q_a=4.5, q_a=6.5 and q_a=7.5 were investigated, both for soft and hard puffing. The density limit was about a factor of two lower for the soft than for the hard puffing discharges. The density was always terminated by increased mode activity with slightly increased loop voltage and plasma resistivity, but without current disruption. The mode frequency initially decreases then increases again. The current was either constant or decreased slightly during the increased mode activity.

A disruption or a density limitation show variety of scenarios but the common factor in all cases is destabilization of the q=2 surface. Large number of these scenarios on TCA with only partial agreement with the observations on JET [7], TFR [20], or other machines, suggest that the physical scenario may differ from machine to machine. The scenario is perhaps sensitive to the aspect ratio or to other geometrical factors even if the final value of density limit remains similar to that described by Greenwald et al. [3] universal formula.

Acknowledgments

The authors thank Dr. M. Dutch for very useful comments in the preparation of this paper. This work was partially supported by the Swiss National Science Foundation.

References

1. MURAKAMI, M., CALLEN, J.D., BERRY, L.A., Nuclear Fusion **16** (1976) 347
2. STOTT, P. E., HUGILL, J., FIELDING, S. J., et al. Controlled Fusion and Plasma Physics **1** (1979) 151
3. GREENWALD, M., TERRY, J., WOLFE, S., et al., "A New Look at Density Limit in Tokamak ", MIT report PFC/JA-86-22 (1988)
4. VERSHKOV, V.A., MIRNOV, S.V., Nucl. Fusion **17** (1972) 383
5. STÄBLER, H., NIEDERMEYER, H., LOCH, R., et al. 16-th Conference on Controlled Fusion and Plasma Physics Venice part **I** (1989) 23
6. BAZDENKOV, S.V., GRISINOV, A.V., POGUTSE, O.P., Plasma Physics and Controlled Fusion **32** (1990) 1061
7. WESSON, J.A., GILL, R.D., HUGON, M., et al., Nuclear Fusion **29** (1989) 641
8. HOLLENSTEIN, CH., DUVAL, B.P. , DUDOK DE WIT, T., et al., J. of Nuclear Materials **176&177** (1990) 343
9. DE CHAMBRIER, A., COLLINS, G.A., HOLLENSTEIN, CH., et al., "Target Plasma Conditions in TCA". CRPP report LRP 241/84 and CHEETHAM, A.D., HAYM, A., HOFMANN, F., et al., 11 Symposium on Fusion Technology, Oxford (1980)
10. RÖHR, H., STEUER, K.-H., MURMANN, MEISEL, H., D., "Periodic Thomson Scattering in ASDEX". IPP report III/121 B
11. JOYE, B., LISTER, J.B., MORET, J.-M., NOWAK, S., Plasma Physics and Controlled Fusion **29** (1987) 27
12. JOYE, B., LISTER, J.B., MORET, J.-M., et al., Plasma Physics and Controlled Fusion **30** (1988) 743

13. NIESWAND, CH., PIETRZYK, Z.A. , POCHELON, A., et al.. 17th Conference on Controlled Fusion and Plasma Heating Amsterdam part **I** (1990) 78

14. HIRSHMAN, S.P., HAWRYLUK, R.J., BRIGE, B., Nuclear Fusion **17** (1977) 611

15. NIESWAND, CH., BEHN, R., SIEGRIST, M.R., et al., 18th Conference on Controlled Fusion and Plasma Heating Berlin part IV (1991) 289

16. RYTER, F., POCHELON, A., HOFMANN, F., 14th Conference on Controlled Fusion and Plasma Heating Madrid part I (1987)

17. MURMANN, H.D., WAGNER, F., BEKER,G., et al., 13-th Conference on Controlled Fusion and Plasma Heating Schliersee (1986) 279

18. TROYON, F., GRUBER, R., SAURENMANN, H., et al., Plasma Phys. and Contr. Fusion **26**, (1984) 209 and TROYON, F., GRUBER, R., Phys. Letters A **100A** (1985) 29

19. EJIMA, S., PETRIE, T.W., ANGEL, T:R:, Nuclear Fusion **22** (1982) 1627

20. TFR GROUP, "Minor and Major Disruptions in the TFR Tokamak" EUR-CEA-FC-1151 (1982)

21. BONDESON, A., PARKER, R., HUGON, M., " MHD Modeling of Density Limit Disruptions in Tokamaks" LRP 429/90 (1990)

22. PERSON, M., BONDESON, A., Phys. Fluids **B2** (1990) 2315

23. HARLEY, T.R., BUCHENAUER, D.A., COONROD, J.W., MCGUIRE, K.M., Nuclear Fusion **29** 5 (1989) 771

24. DUVAL, B.P., JOYE, B., MARCHAL, B., 18th Conference on Controlled Fusion and Plasma Heating Berlin part II (1991) 37

25. FIELD, A.R., FUSSMANN, G., HOFMANN, J.V., "Measurements of Radial Electric Field in the ASDEX Tokamak" IPP III/165 (1990)

26. DUPERREX, P. A., HOLLENSTEIN, CH., JOYE, B., et al., Phys. Letter **106A** p.133 (1984) and MALACARNE, M., DUPERREX, P. A., Nucl. Fusion **27** (1987) 2113

27. MATSUMOTO, H., BURRELL, K.H., CARLSTROM, T.N., et al., "Suppression of the Edge Turbulance at the L-H Transition in DIII-D" GA-A20383 (1991) and GOHIL,P., BURRELL, K.H., DOYLE, E.J., et al., 18th Conference on Controlled Fusion and Plasma Heating Berlin part I (1991) 289

28. FURTHH, P., KILEEN, J., ROSENBLUTH, M.N., Phys. Fluids **6** (1963) 459

29. BONDESON, A., "Disruptions in Tokamaks" International School of Fusion and Plasma Physics. Varenna (1987)

30. REMKES, G.J.J.,SCHÜLLER, F.C., Plasma Physics and Controlled Fusion **33** (1991) 181

shot: 41888

time (ms)	*n*	*m*	*q*	*f* (kHz)	comments
85–95	1	2	2	12.7	
100–105	1	2	2	15.1	
	2	3	1.5	30.8	
120–125	1	2	2	16.6	
	2	3	2	32.7	
150–155	1	2	2	13.2	
	2	4–5	2–2.5	26.4	modes 3,1 and 5,2 may also be present with 10 and 35 kHz
156.5–157.8	–	–	–	–	modes speed up rapidly

Table I: Magnetic oscillations mode numbers for hard puffing.

shot: 41890

time (ms)	*n*	*m*	*q*	*f* (kHz)	comments
74–79	1	2	2	12.2	very low level
104–109	1	2	2	13.7	
122–127	1	2	2	13.7	$m = 4$ mode may also be present
	2	5	2.5	27.8	
133–138	1	2	2	13.7	
	2	3	1.5	25.4	
141–146	1	2	2	8.8	
	2	4	2	16.6	
	3	6	2	25.9	
149–154	1	2	2	6.3	
	2	4	2	12.2	
	3	6	2	20.5	

Table II: Magnetic oscillations mode numbers for soft puffing.

property	soft puffing	hard puffing
current density	less peaked	more peaked
electron density	parabola	flat → peaked
temperature profile	peaked	peaked
pressure profile	peaked	less peaked
mode amplitude	very low → high	finite not growing
mode frequency	13-5 kHz	13-18 kHz
line average density achieved	$(4\text{–}5) \times 10^{13}\text{cm}^{-3}$	$1.1 \times 10^{14}\ \text{cm}^{-3}$
β_T at the density limit	25% of Troyon limit	~ 60% of Troyon limit

Table III: Differences between soft and hard puffing.

Figure Captions

Fig. 1. The Thomson scattering system.

DM - Diamagnetic mirror

BM - Brewster window

Fig. 2. Time dependence of plasma parameters for soft and hard puffing:

(a) soft X-ray signal from diode looking on a whole plasma cross section

(b) $\beta + l_i/2$,

(c) Mirnov mode activity (envelope of signal),

(d) gas valve voltage.

Fig. 3. Transition between soft and hard puffing:

(a) Δx-ray is the difference between the soft x-ray maximum during the puff and the soft x-ray signal before puffing as a function of gas particle flux to the vacuum chamber,

(b) change of $\beta + l_i/2$ at the same time.

Fig. 4. Typical hard puffing discharge characteristics (shot 39117):

(a) total plasma current and loop voltage,

(b) line averaged density,

(c) $\beta + l_i/2$,

(d) ion temperature,

(e) flux of particles injected into the vacuum chamber.

Fig. 5. Additional characteristics of hard puffing discharges, same discharge programming as in Fig. 4:

(a) central and volume averaged electron temperature measured by Thomson scattering and soft X-ray emission,

(b) peaking factor for electron density profile measured by Thomson scattering and FIR interferometer,

(c) toroidal beta calculated from Thomson scattering profiles and measured central ion temperature with assumption of similar electron and ion temperature profiles and $Z_{eff} = 1.3$,

(d) plasma inductance calculated from Thomson profiles with neo-classical resistivity and the diamagnetic signal,

(e) flux of particles injected into the vacuum chamber.

Fig. 6. Electron temperature profiles measured by Thomson scattering at various times during hard puffing discharges:

$t = 75$ ms (before hard puffing),
$t = 87$ ms (maximum temperature),
$t = 100$ ms (flattest density profile),
$t = 165$ ms (just before disruption).

Fig. 7. Electron density profiles measured by Thomson scattering at various times during hard puffing discharges. See caption for Fig. 6 for times.

Fig. 8. Global parameters of hard puffing discharges:

(a) total electron energy,
(b) total plasma energy.
(c) electron energy confinement time
(d) total energy confinement time

Fig. 9. Frequency spectra of the magnetic oscillations at two different times in hard puffing discharge:

$t = 75$ ms before hard puffing,
$t = 82$ ms near the maximum plasma temperature.

Fig. 10. Intensity of the high frequency oscillations ($f = 560$ kHz) and Mirnov oscillations as a function of time at the beginning of hard puffing. Gas puff starts at t = 75 ms.

Fig. 11. Total plasma radiation as a function of time together with ohmic power for a less clean plasma (more than 500 shots after boronisation) and radiation profiles as a function of time.

Fig. 12. Total radiation as a function of time together with ohmic power for a clean plasma (100 shots after boronisation) and radiation profiles as a function of time.

Fig. 13. Relative temperature, density and pressure profiles before disruption for soft and hard puffing cases. The figure shows the best fit to the data for both hard and soft puffing, the points represent average over 4 shots. Points are shown for both soft and hard puffing on graph 13b. On 13a and 13c only the soft puffing points are shown to keep the figures more readable.

Fig. 14. Electron and total plasma energy as a function of line density.
o soft puffing, • hard puffing.

Fig. 15. Electron energy confinement time as a function of line density. Plasma energy confinement time as a function of density from Thomson scattering, diamagnetic signal and a few points from $\beta_p + l_i/2$ with l_i calculated from the temperature profile.

Fig. 16. Hugill and Troyon diagrams. The squares are shots with mode limited density, the triangles are disruption limited shots, circles are points measured at various times during hard puffing discharges.

Fig. 17. Current, loop voltage and mode activity before and during disruption at $q_a = 2.4$.

Fig. 18. Temperature (a) and density (b) profile just before disruption for $q_a = 2.4$ (shot 42658).

Fig. 19. Comparison of current and loop voltage for soft and hard puffing disruptions at $q_a = 3.2$ (shots 40366 and 39858).
(a,b) soft puffing
(c,d) hard puffing

Fig. 20. Temperature profiles before and at two different times after disruption, taken from different discharges. After disruption shots 41892 and 41865 ($q_a = 3.2$).

Fig. 21. (a) central electron temperature from soft x-rays during a disruption (one point of Thomson scattering is also indicated)

(b) plasma current and mode amplitude as a function of time for the same shot (40366).

Fig. 22. Contour plots of the amplitudes of frequency versus time of amplitude contour plots for soft a) and b) hard puffing before disruption. The associated (m,n) mode numbers are given in brackets.

Fig. 23. Magnetic oscillations prior to disruption in hard puffing showing the frequency increase a few cycles before the time of disruption (shot 41888). The current starts to decay at t=160 ms for this shot.

Fig. 24. Frequency spectra of Mirnov activity:

(a) soft puffing showing large second harmonic,

(b) hard puffing a broader spectrum of frequencies

Fig. 25. Magnetic oscillations in a hard puffing discharge, which exhibit beating of several frequencies.

Fig. 26 Mode amplitude as a function of time for soft puffing (shot 40366) and hard puffing (shot 41888) discharges.

Fig. 27. Carbon V Doppler shift measurement of the toroidal (a) and poloidal (b) plasma rotational velocity versus time during a hard puffing discharge. Gas puff starts at 75 ms. Dashed lines indicate the approximate average rotation speed without gas puffing.

Fig. 28. Soft x-ray traces for: a) soft puffing discharge without sawtooth activity and b) for hard puffing discharge showing the sawteeth after puffing starts at 70 ms for these shots.

Fig. 29. Current profiles at various times during hard puffing discharges calculated from temperature and density profiles assuming neoclassical plasma conductivities and $q \approx 1$ in the plasma centre. The q=1 radius is calculated

from the total plasma current. The current profile is seen to shrink during hard puffing. This observation is also supported by Fig. 5d and Fig. 28.

Fig. 30. Soft x-ray sawtooth activity before disruption for q_a = 3.2 presented on two different time scales. Shrinking of the q=1 radius is visible (top figure), as well as the onset of the disruption near r=14 cm, which is approximate location of the q=2 surface (bottom figure).

Fig. 31. Plot of plasma inductance versus q_a showing stable and unstable regions. Experimental stability boundary for soft puffing. The maximum possible inductance is assumed to be the inductance of a flat current located inside the $q=1$ surface and no current outside.

Fig. 32. a) Mode frequency versus time for $q_a = 4.5$ (isoplot), shot 41858. In brackets are the (m,n) mode numbers.

b) Current [kA], loop voltage [V*30], line averaged density [10^{12} cm^{-3}], gas flux [$\Phi g*2*10^{18}$] and mode activity.

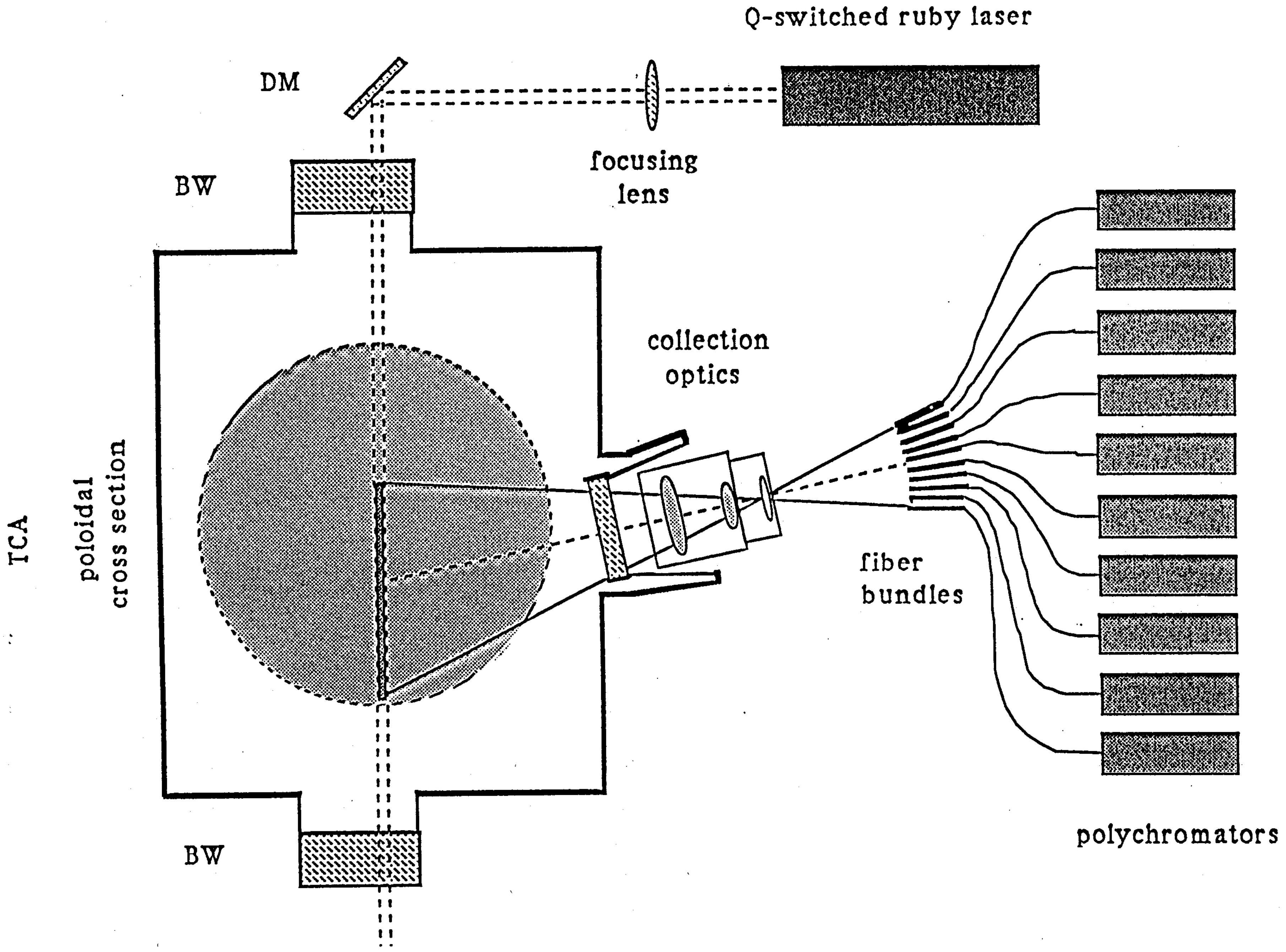
Q-switched ruby laser
DM
focusing lens
BW
collection optics
TCA
poloidal cross section
fiber bundles
BW
polychromators

Figure 1

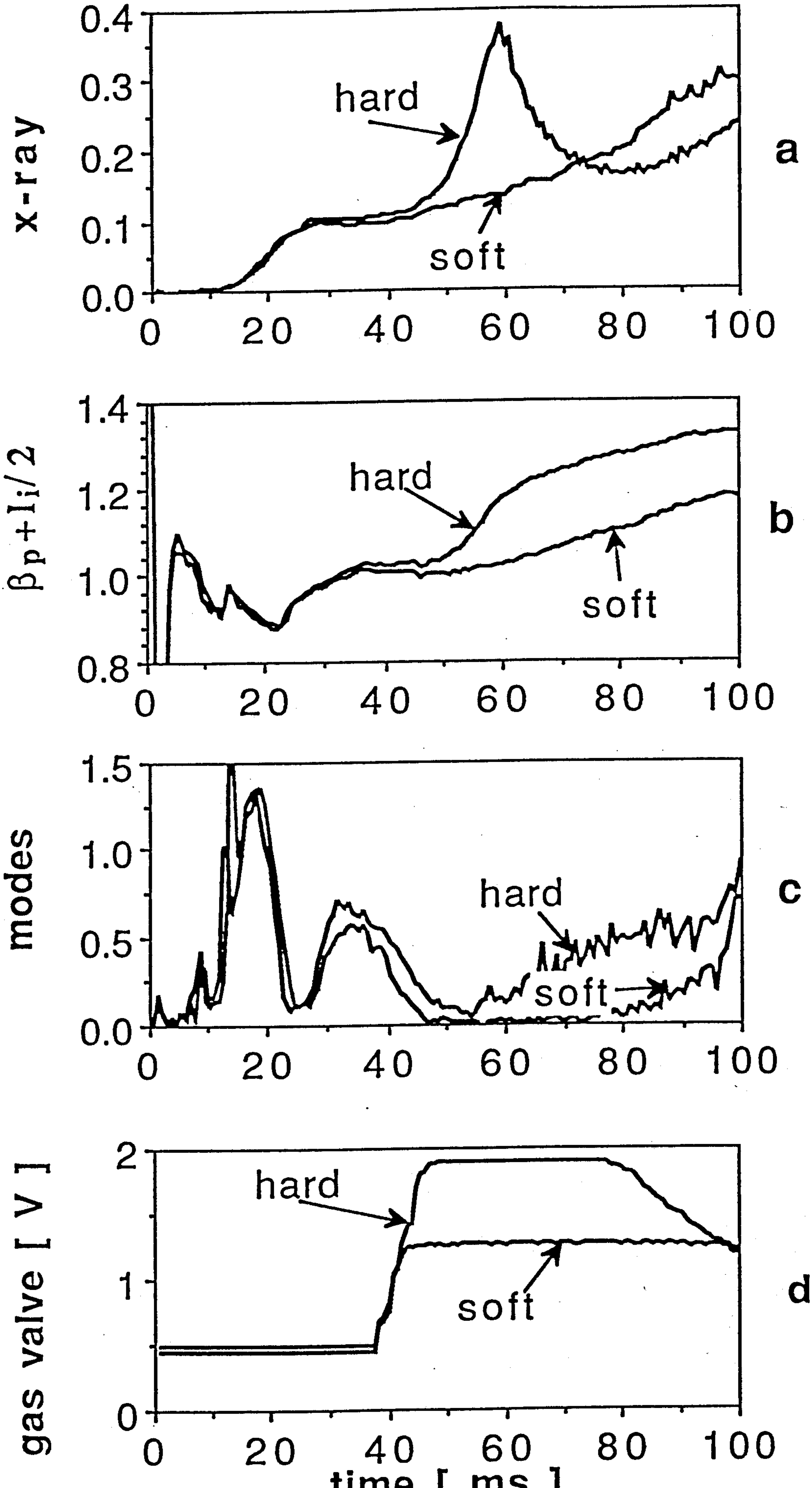
x-ray
0.4
0.3
0.2
0.1
0.0
0
20
40
60
80
100
hard
soft
a
$\beta_p + l_i/2$
1.4
1.2
1.0
0.8
0
20
40
60
80
100
hard
soft
b
modes
1.5
1.0
0.5
0.0
0
20
40
60
80
100
hard
soft
c
gas valve [V]
2
1
0
0
20
40
60
80
100
hard
soft
d
time [ms]

Figure 2

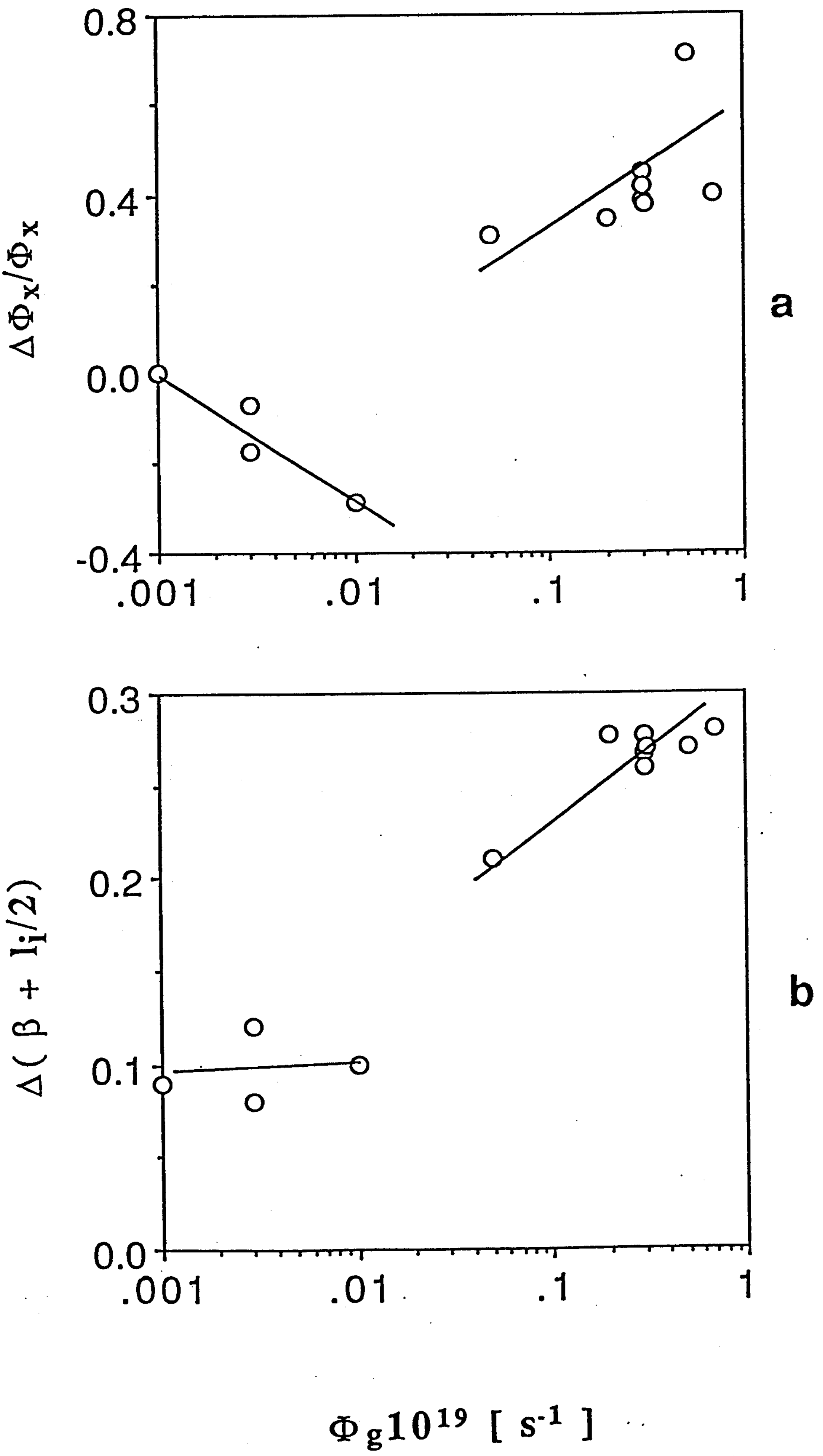
0.8
0.4
0.0
-0.4
$\Delta\Phi_x/\Phi_x$
a
.001
.01
.1
1
0.3
0.2
0.1
0.0
$\Delta(\beta + l_i/2)$
b
.001
.01
.1
1
$\Phi_g 10^{19}$ [s^{-1}]

Figure 3

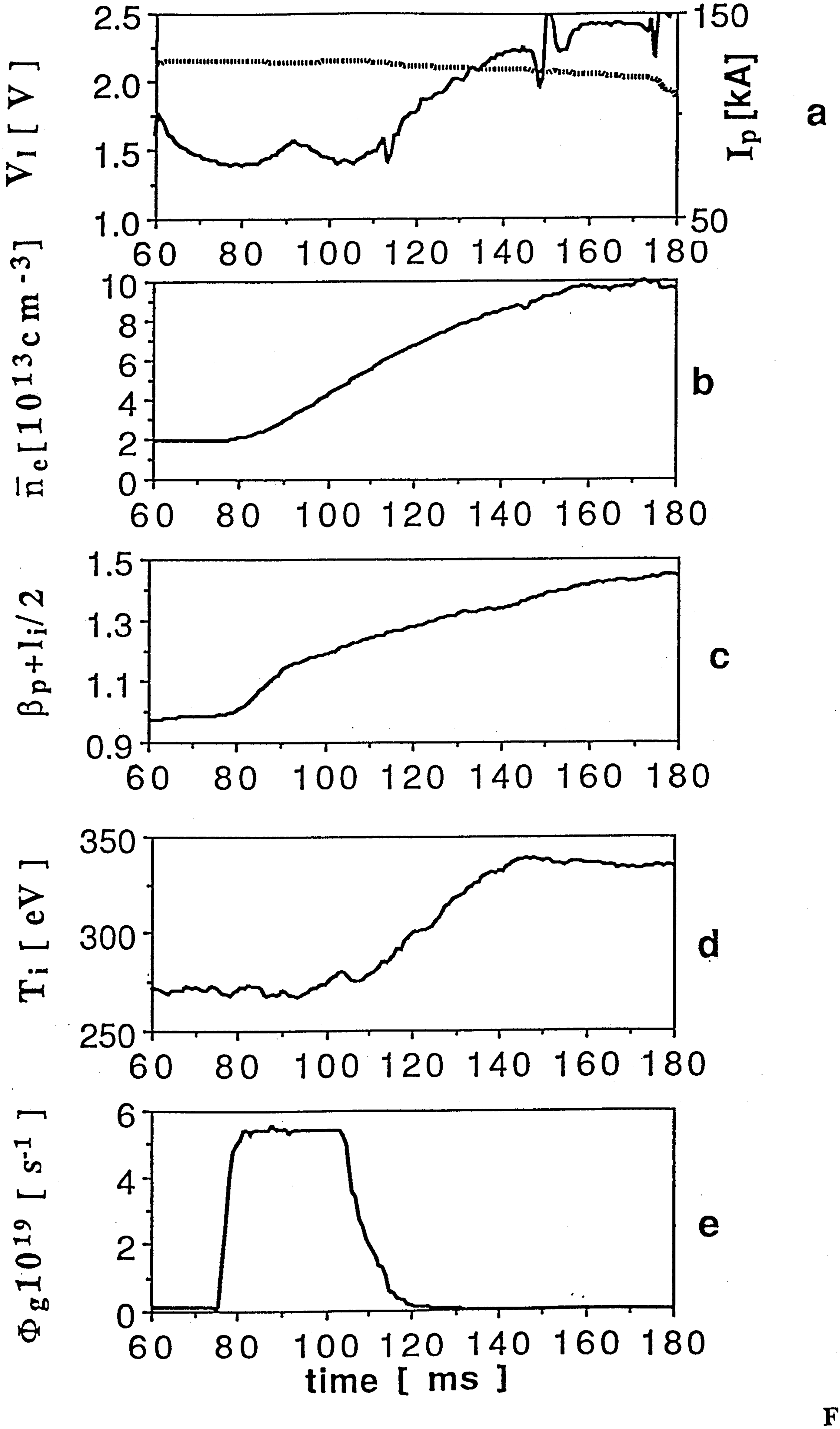

V_l [V]
2.5
2.0
1.5
1.0
150
50
I_p [kA]
a
60
80
100
120
140
160
180
$\bar{n}_e [10^{13} cm^{-3}]$
10
8
6
4
2
0
b
$\beta_p + l_i/2$
1.5
1.3
1.1
0.9
c
T_i [eV]
350
300
250
d
$\Phi_g 10^{19}$ [s^{-1}]
6
4
2
0
e
time [ms]

Figure 4

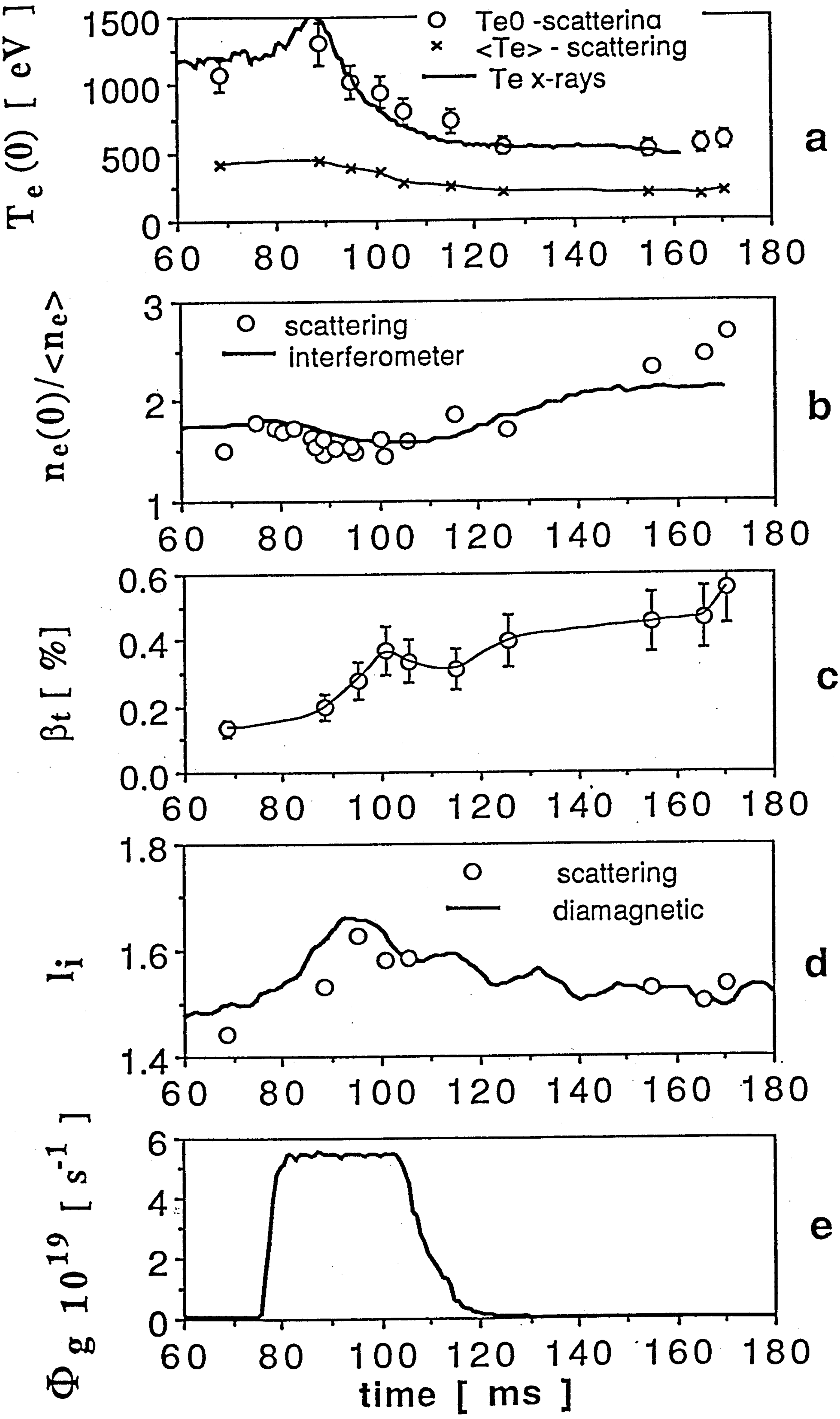
T e (0) [eV]
1500
1000
500
0
Te0 -scattering
<Te> - scattering
Te x-rays
a
ne(0)/<ne>
3
2
1
scattering
interferometer
b
βt [%]
0.6
0.4
0.2
0.0
c
li
1.8
1.6
1.4
scattering
diamagnetic
d
Φg 10^19 [s^-1]
6
4
2
0
e
60
80
100
120
140
160
180
time [ms]

Figure 5

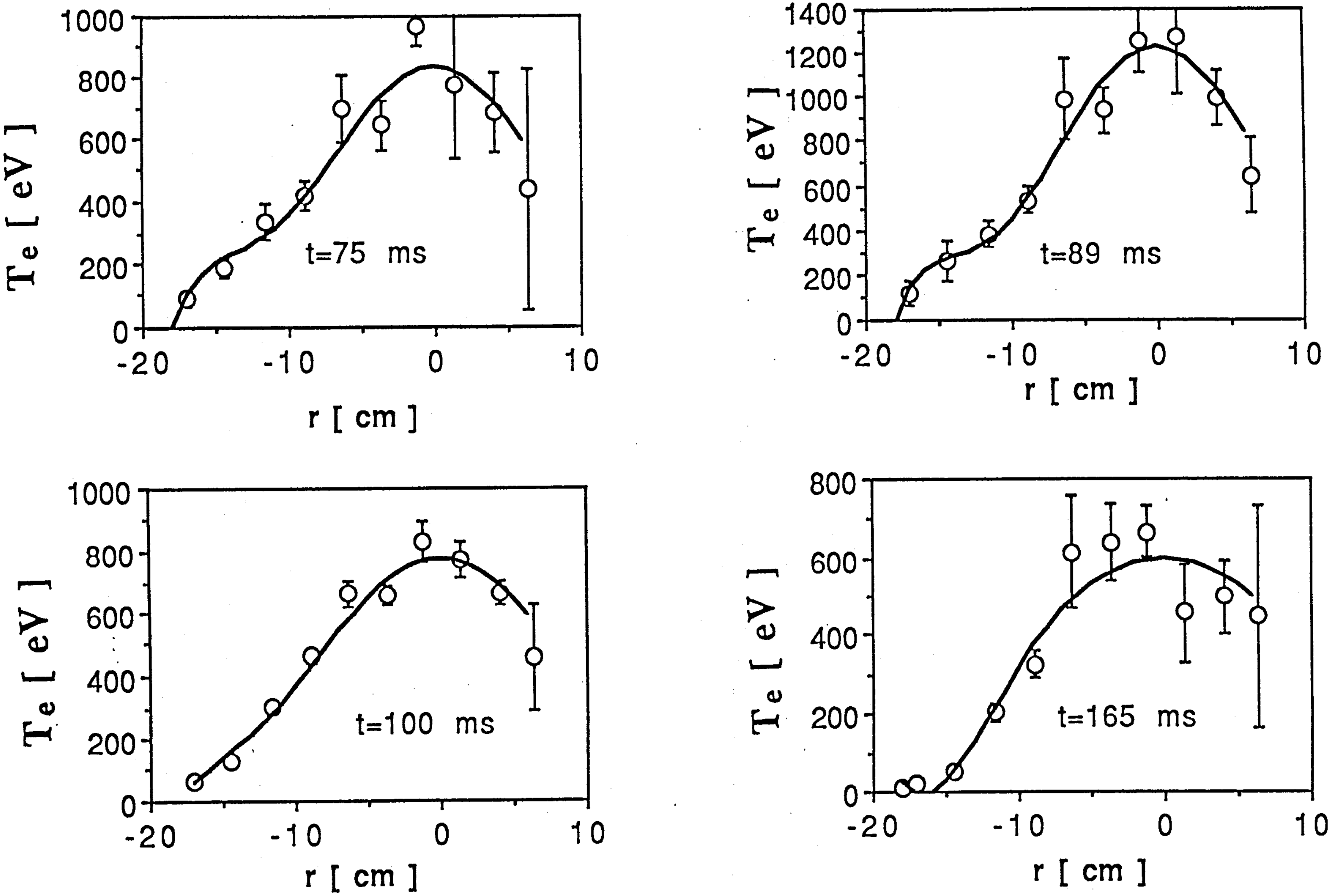
1000
800
600
400
200
0
-20
-10
0
10
T_e [eV]
r [cm]
t=75 ms
1400
1200
1000
800
600
400
200
0
-20
-10
0
10
T_e [eV]
r [cm]
t=89 ms
1000
800
600
400
200
0
-20
-10
0
10
T_e [eV]
r [cm]
t=100 ms
800
600
400
200
0
-20
-10
0
10
T_e [eV]
r [cm]
t=165 ms

Figure 6

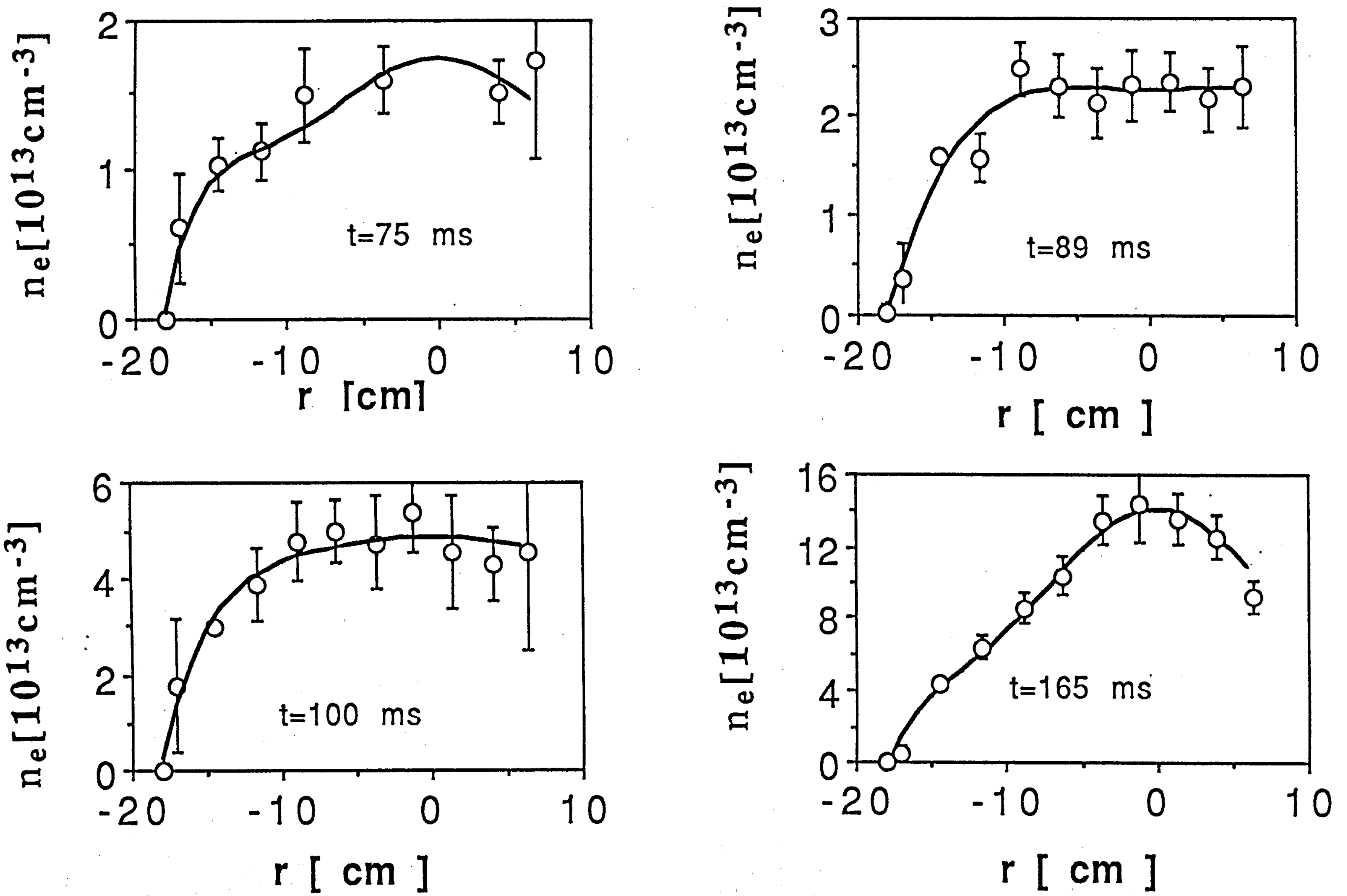
$n_e[10^{13}cm^{-3}]$
0
1
2
-20
-10
0
10
r [cm]
t=75 ms
$n_e[10^{13}cm^{-3}]$
0
1
2
3
-20
-10
0
10
r [cm]
t=89 ms
$n_e[10^{13}cm^{-3}]$
0
2
4
6
-20
-10
0
10
r [cm]
t=100 ms
$n_e[10^{13}cm^{-3}]$
0
4
8
12
16
-20
-10
0
10
r [cm]
t=165 ms

Figure 7

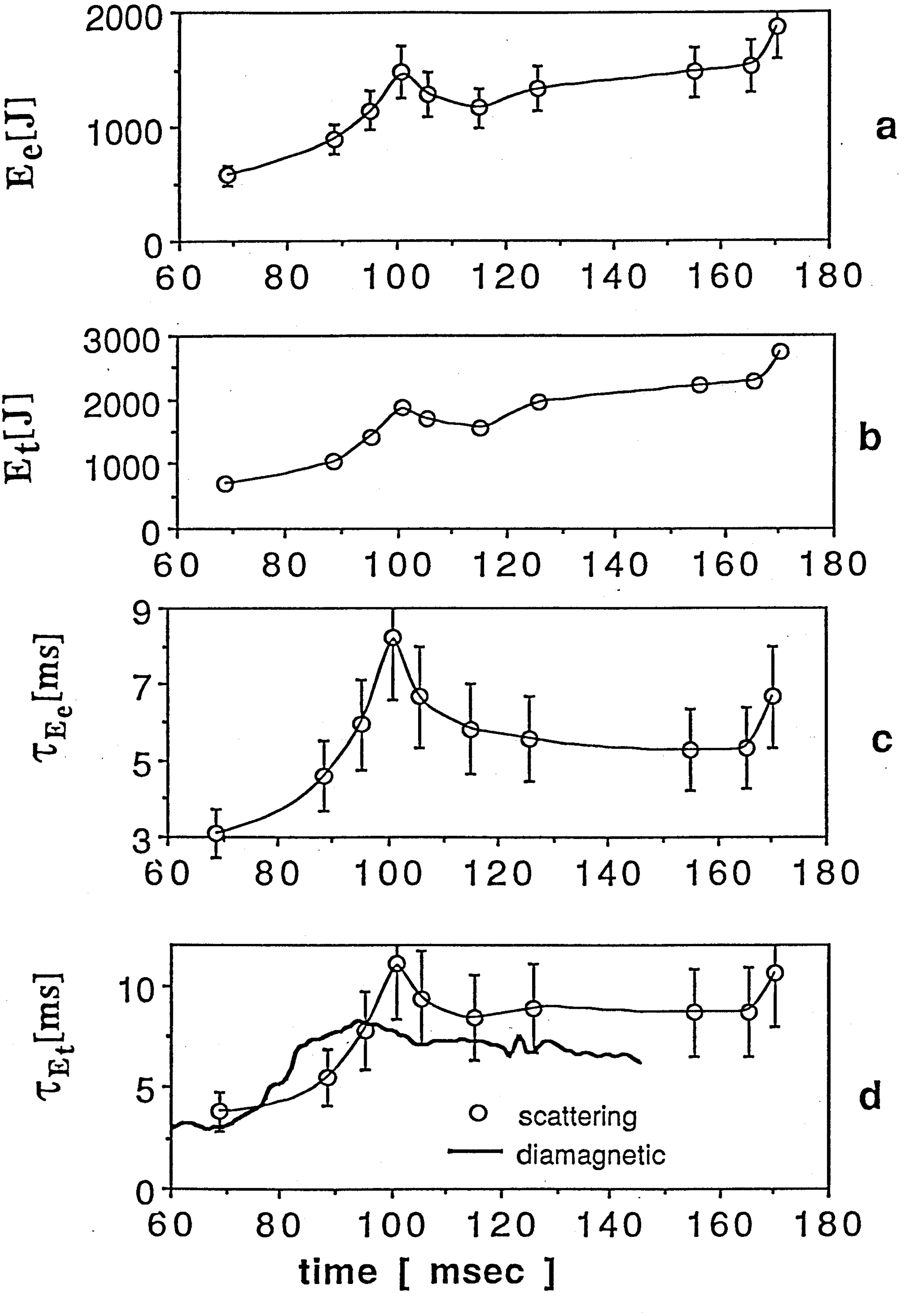
E_e[J]
2000
1000
0
60
80
100
120
140
160
180
a
E_t[J]
3000
2000
1000
0
60
80
100
120
140
160
180
b
τ_{E_e}[ms]
9
7
5
3
60
80
100
120
140
160
180
c
τ_{E_t}[ms]
10
5
0
scattering
diamagnetic
60
80
100
120
140
160
180
d
time [msec]

Figure 8

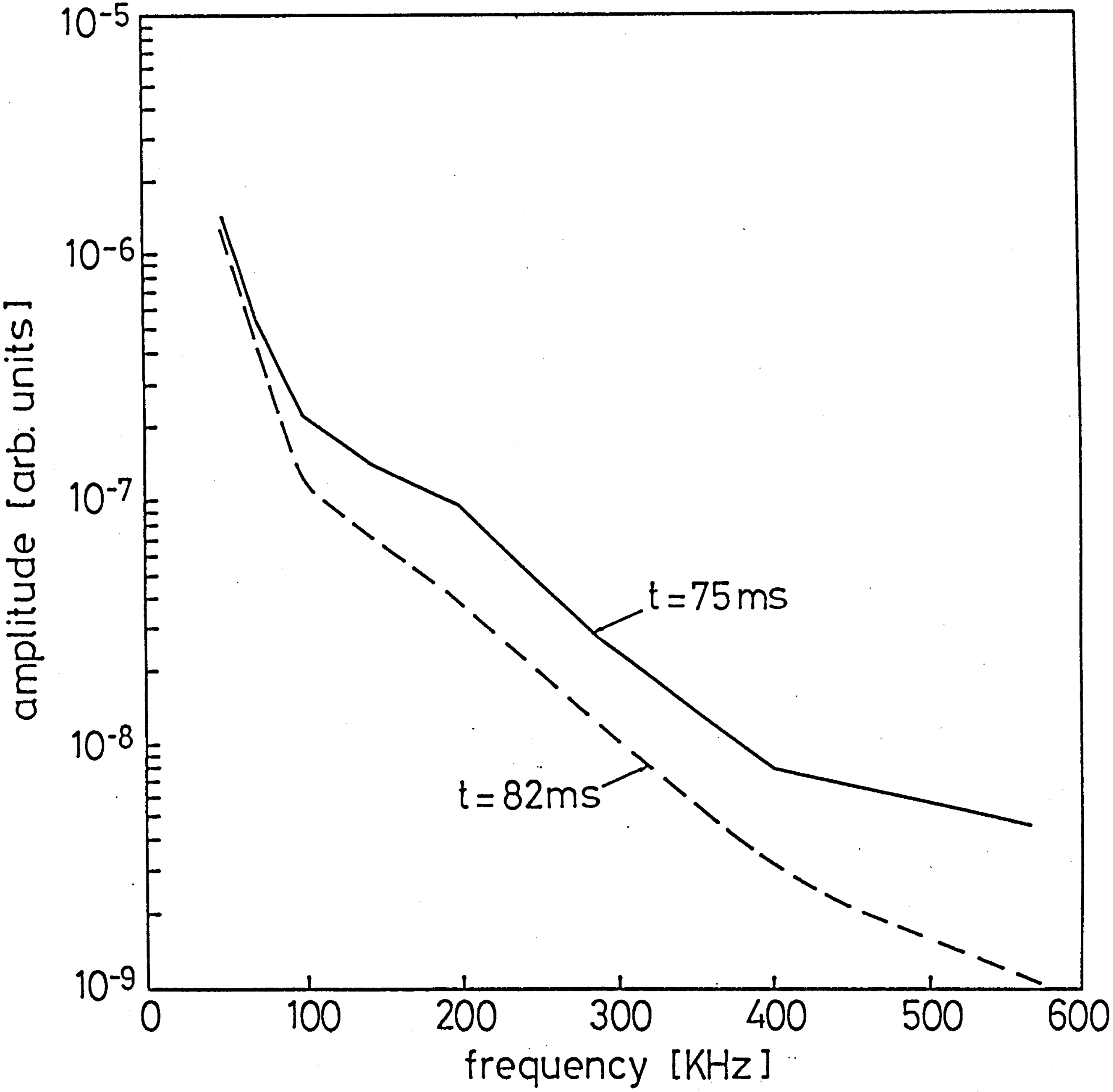
10-5
10-6
10-7
10-8
10-9
amplitude [arb. units]
0
100
200
300
400
500
600
frequency [KHz]
t = 75 ms
t = 82ms

Figure 9

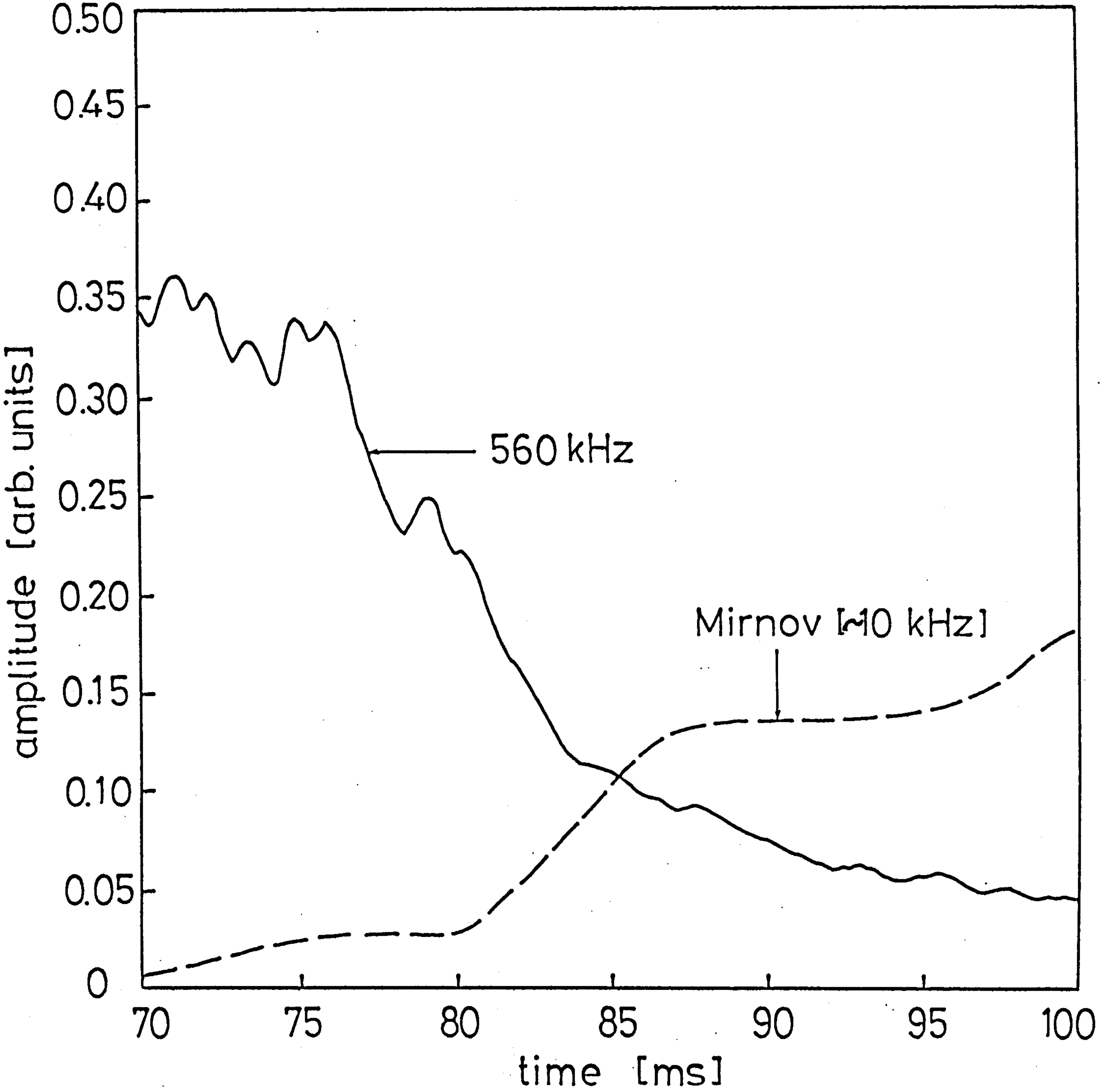
0.50
0.45
0.40
0.35
0.30
0.25
0.20
0.15
0.10
0.05
0
amplitude [arb. units]
70
75
80
85
90
95
100
time [ms]
560 kHz
Mirnov [~10 kHz]

Figure 10

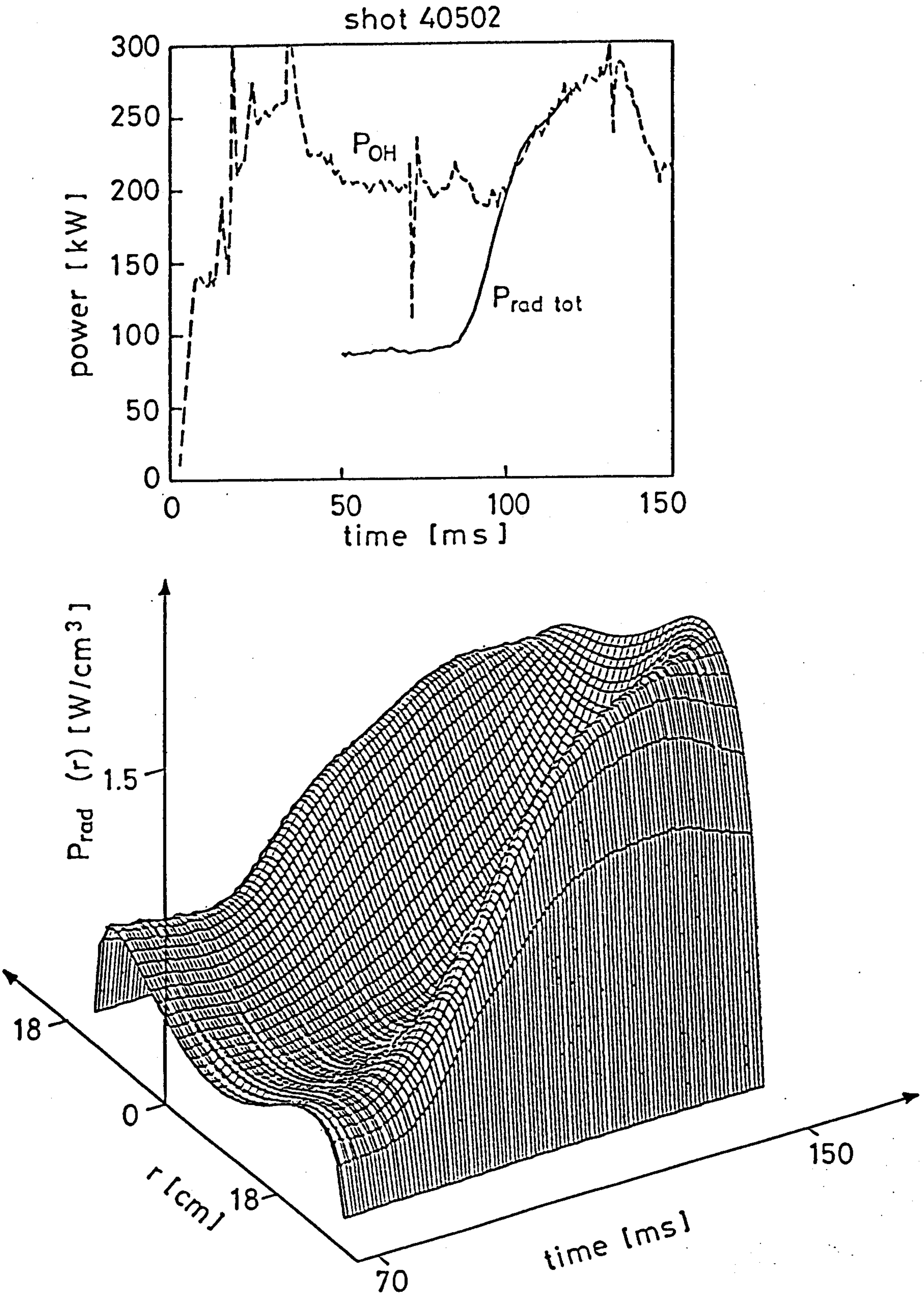
shot 40502
power [kW]
300
250
200
150
100
50
0
0
50
100
150
time [ms]
P_{OH}
$P_{rad\ tot}$
P_{rad} (r) [W/cm^3]
1.5
18
0
r [cm]
18
70
150
time [ms]

Figure 11

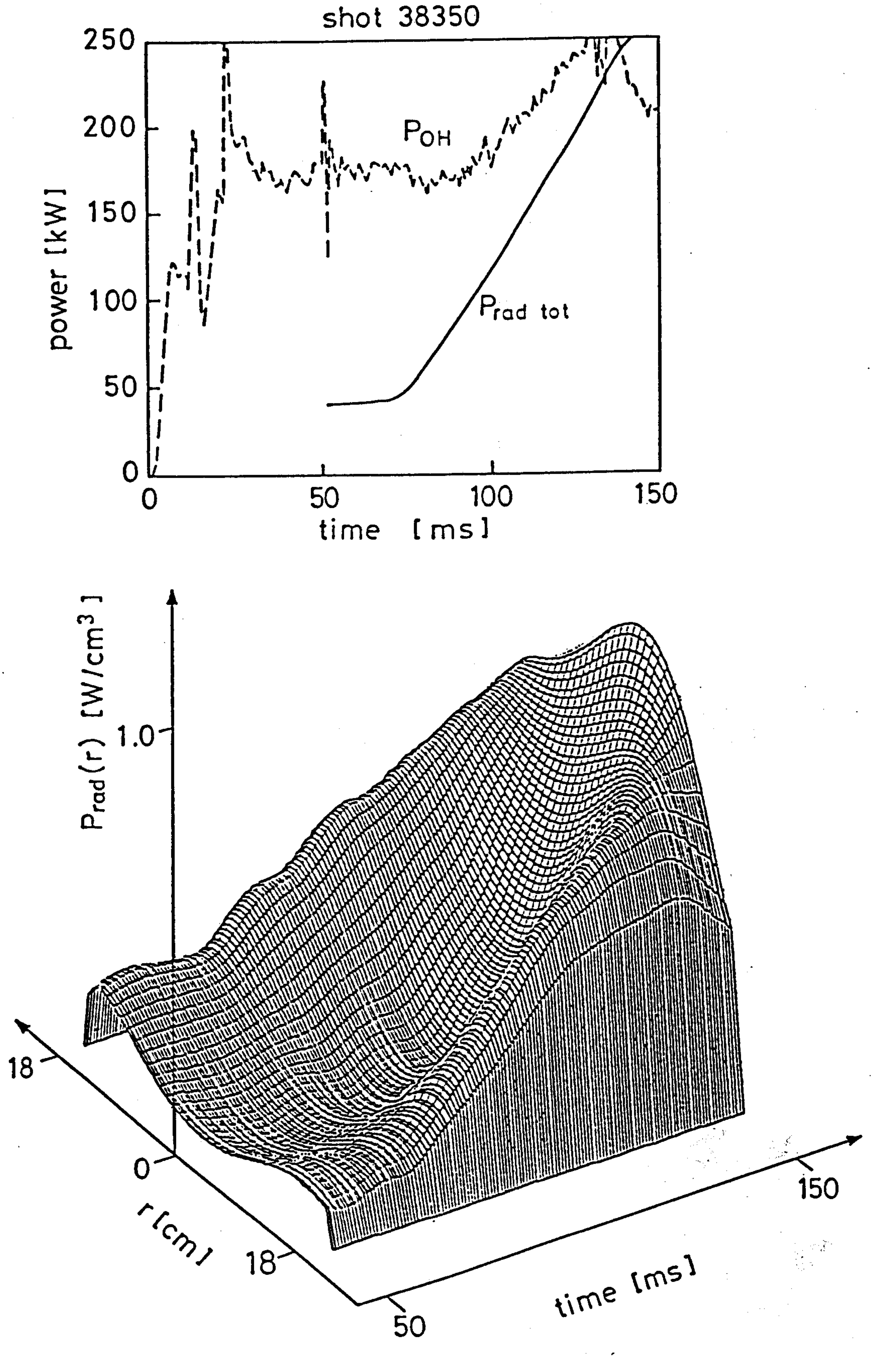
shot 38350
power [kW]
250
200
150
100
50
0
0
50
100
150
time [ms]
P_{OH}
$P_{rad\ tot}$
$P_{rad}(r)$ [W/cm^3]
1.0
18
0
r [cm]
18
50
150
time [ms]

Figure 12

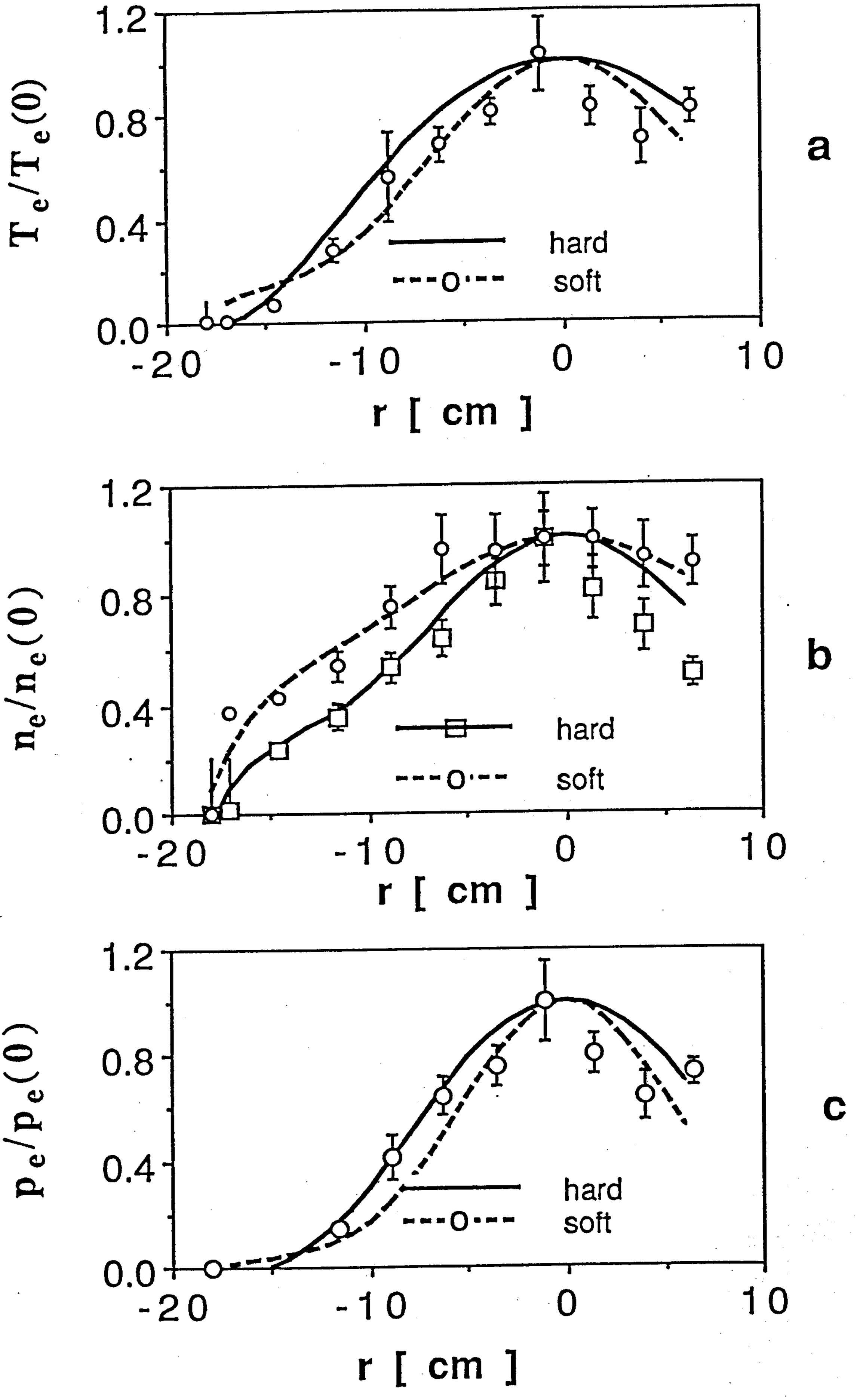
T_e/T_e(0)
1.2
0.8
0.4
0.0
-20
-10
0
10
r [cm]
hard
soft
a
n_e/n_e(0)
1.2
0.8
0.4
0.0
-20
-10
0
10
r [cm]
hard
soft
b
p_e/p_e(0)
1.2
0.8
0.4
0.0
-20
-10
0
10
r [cm]
hard
soft
c

Figure 13

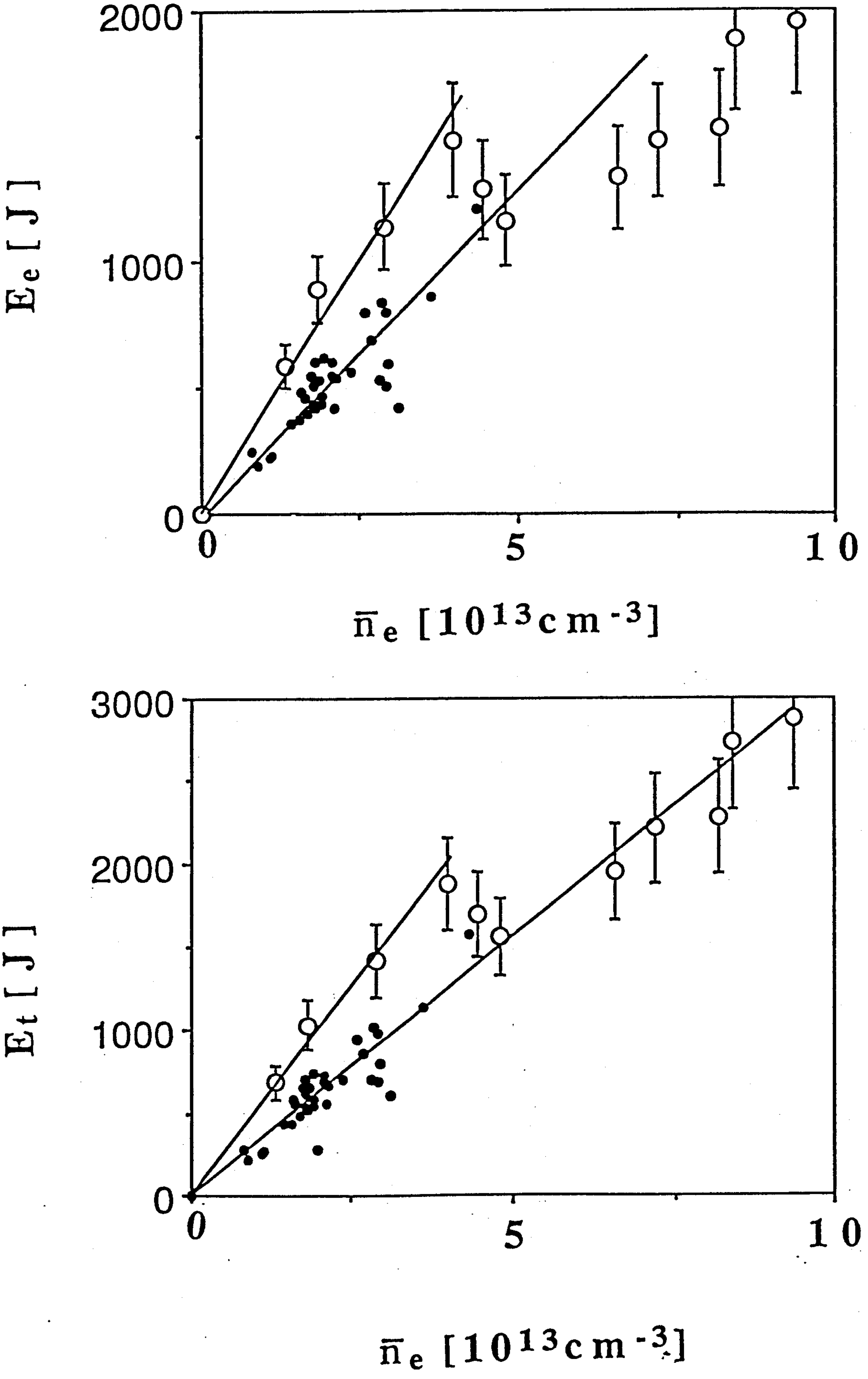
2000
1000
0
E_e [J]
0
5
10
$\bar{n}_e$ [10^{13}cm^{-3}]
3000
2000
1000
0
E_t [J]
0
5
10
$\bar{n}_e$ [10^{13}cm^{-3}]

Figure 14

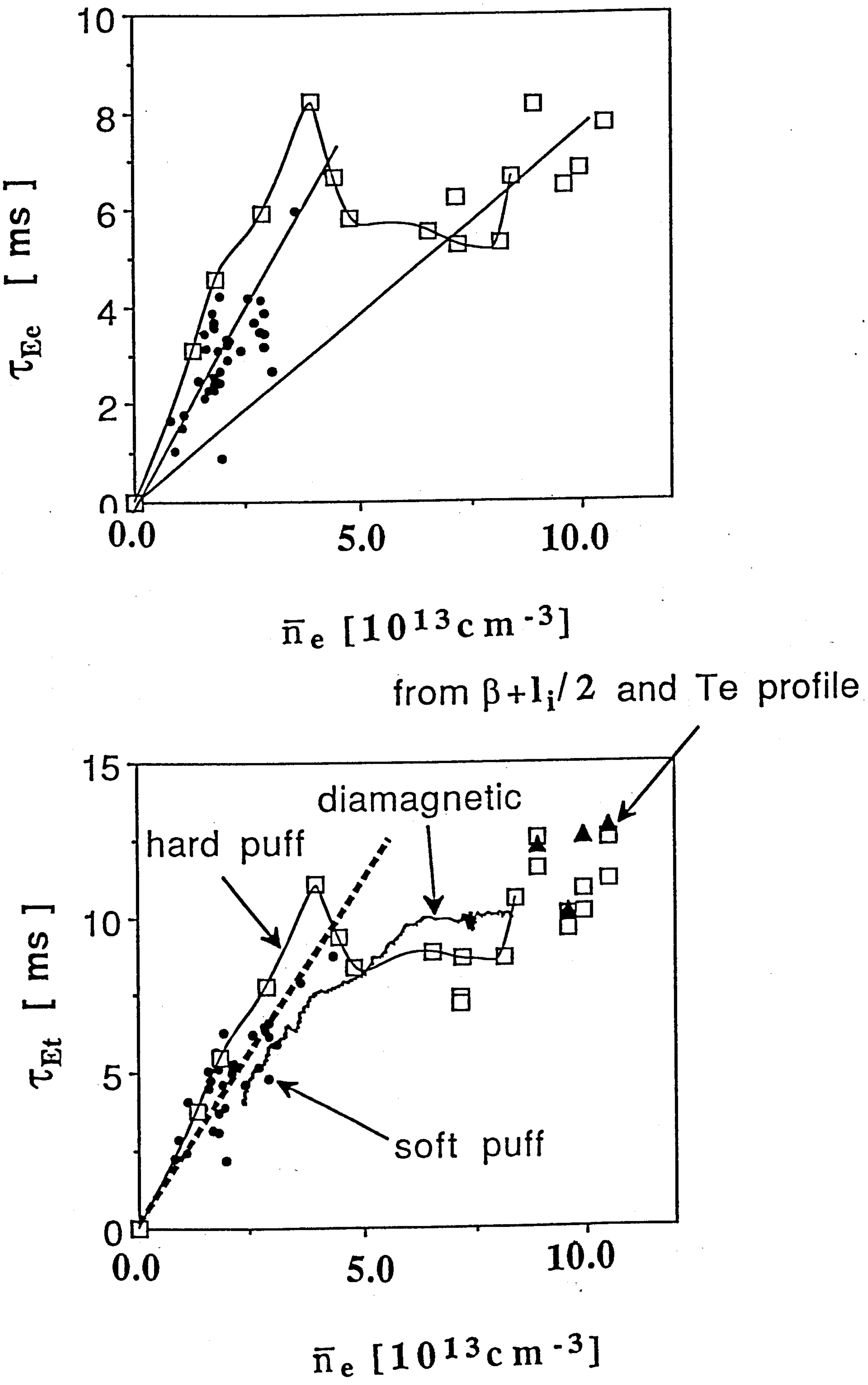
10
8
6
4
2
0
τ_{Ee} [ms]
0.0
5.0
10.0
$\bar{n}_e$ [10^{13}cm^{-3}]
from $\beta+l_i/2$ and Te profile
15
10
5
0
τ_{Et} [ms]
diamagnetic
hard puff
soft puff
0.0
5.0
10.0
$\bar{n}_e$ [10^{13}cm^{-3}]

Figure 15

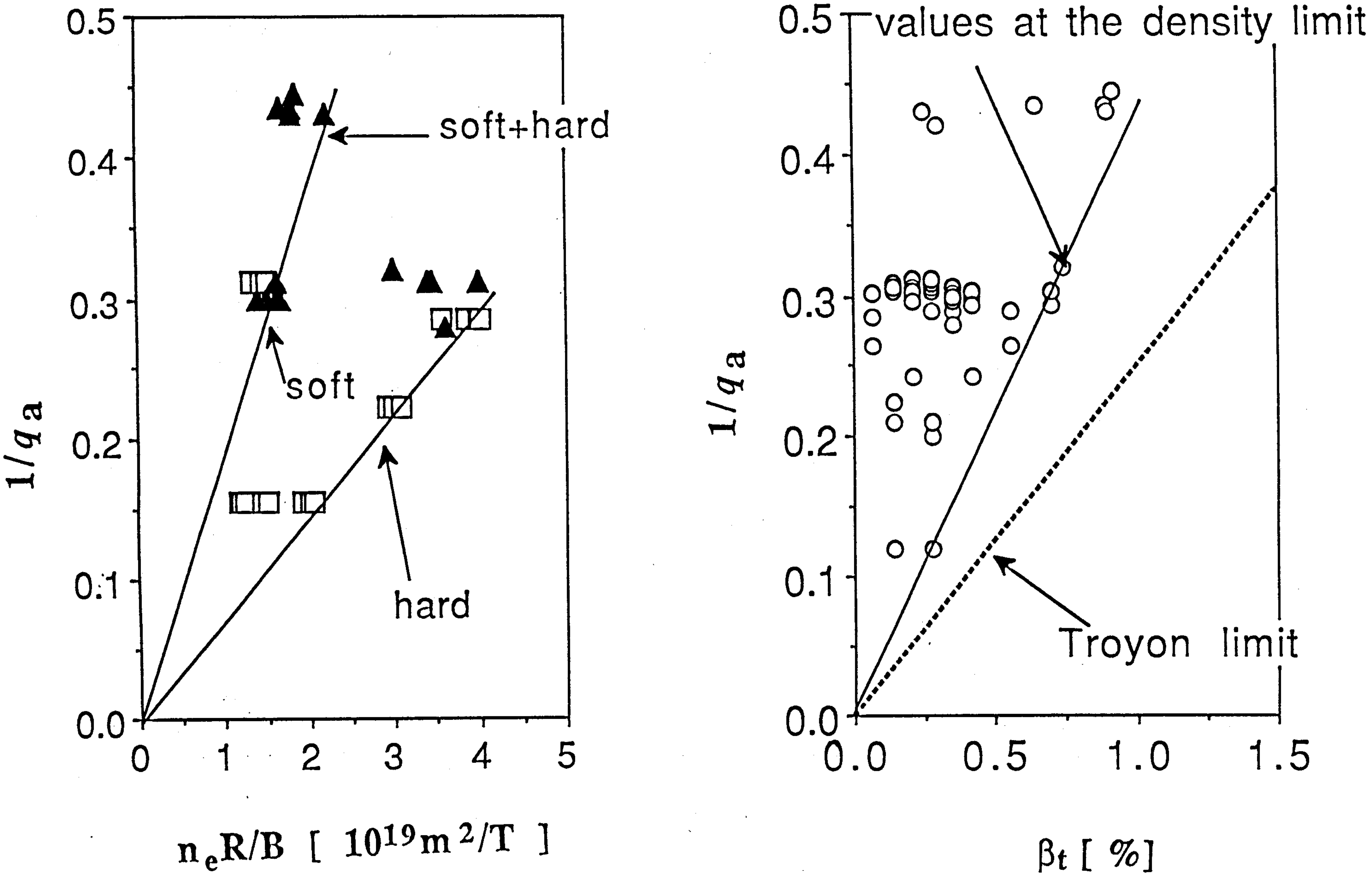
0.5
0.4
0.3
0.2
0.1
0.0
$1/q_a$
soft+hard
soft
hard
0
1
2
3
4
5
n_eR/B [$10^{19} m^2/T$]
values at the density limit
Troyon limit
0.0
0.5
1.0
1.5
β_t [%]

Figure 16

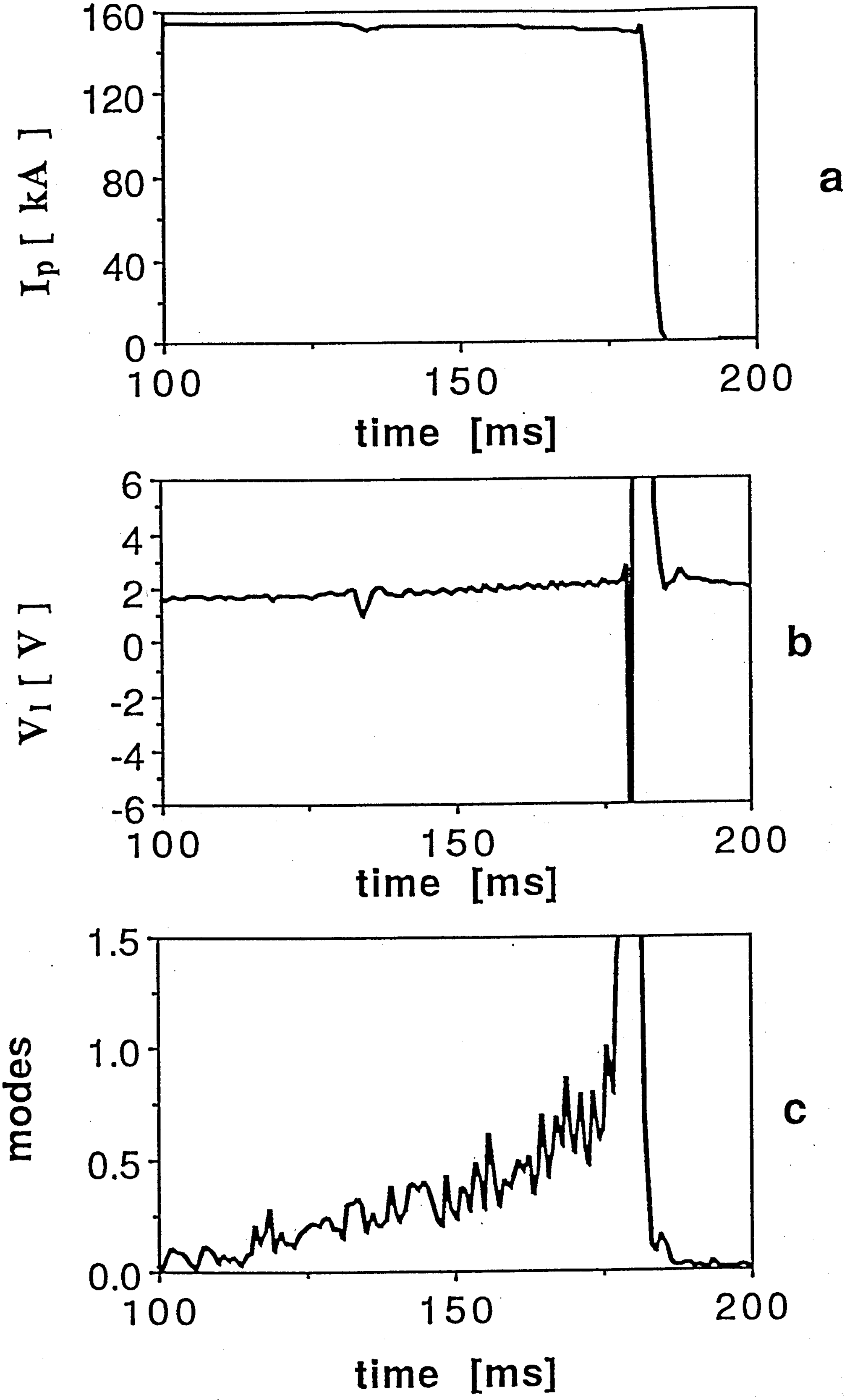
160
120
80
40
0
Ip [kA]
100
150
200
time [ms]
a
6
4
2
0
-2
-4
-6
VI [V]
100
150
200
time [ms]
b
1.5
1.0
0.5
0.0
modes
100
150
200
time [ms]
c

Figure 17

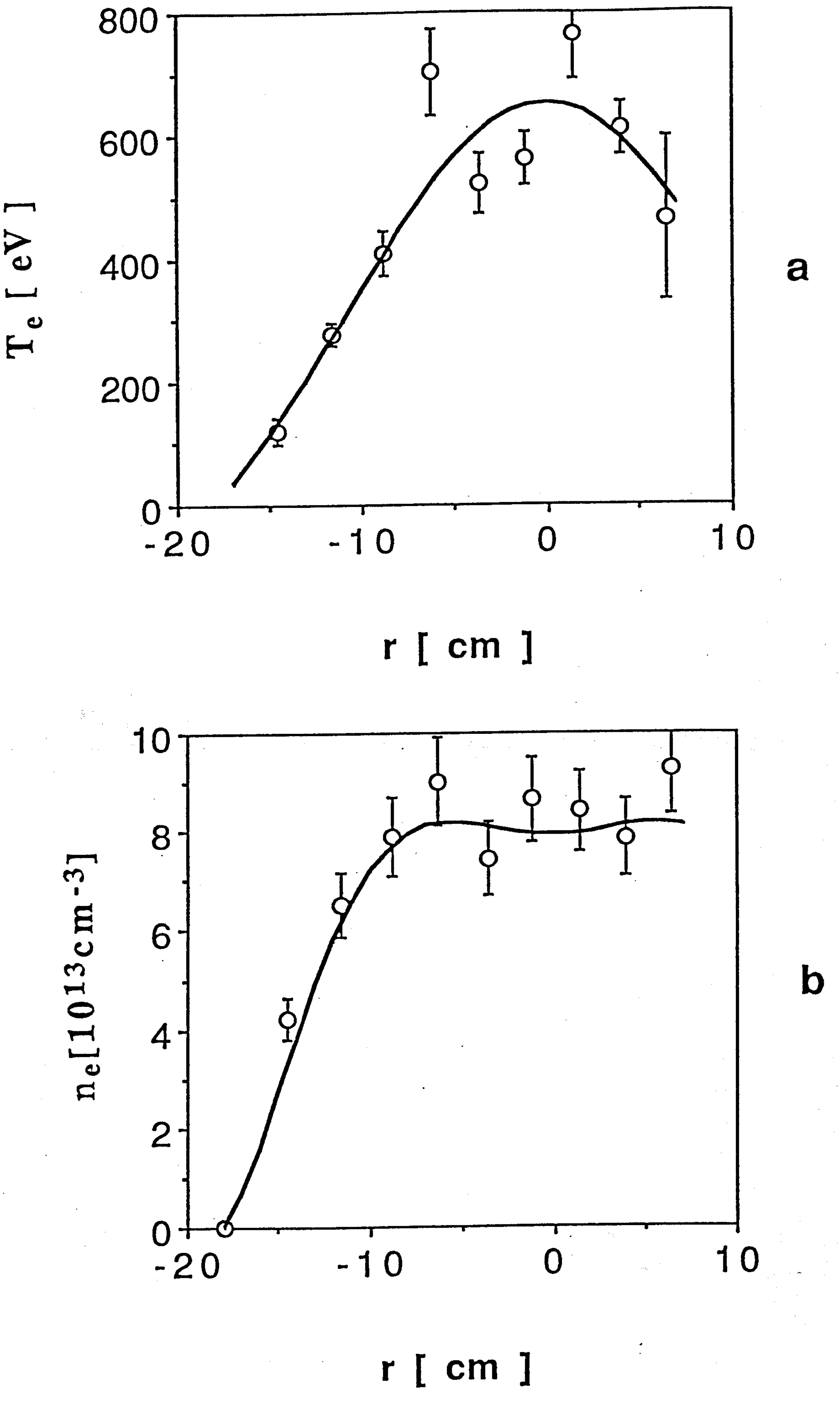

800
600
400
200
0
T_e [eV]
-20
-10
0
10
r [cm]
a
10
8
6
4
2
0
$n_e[10^{13}cm^{-3}]$
-20
-10
0
10
r [cm]
b

Figure 18

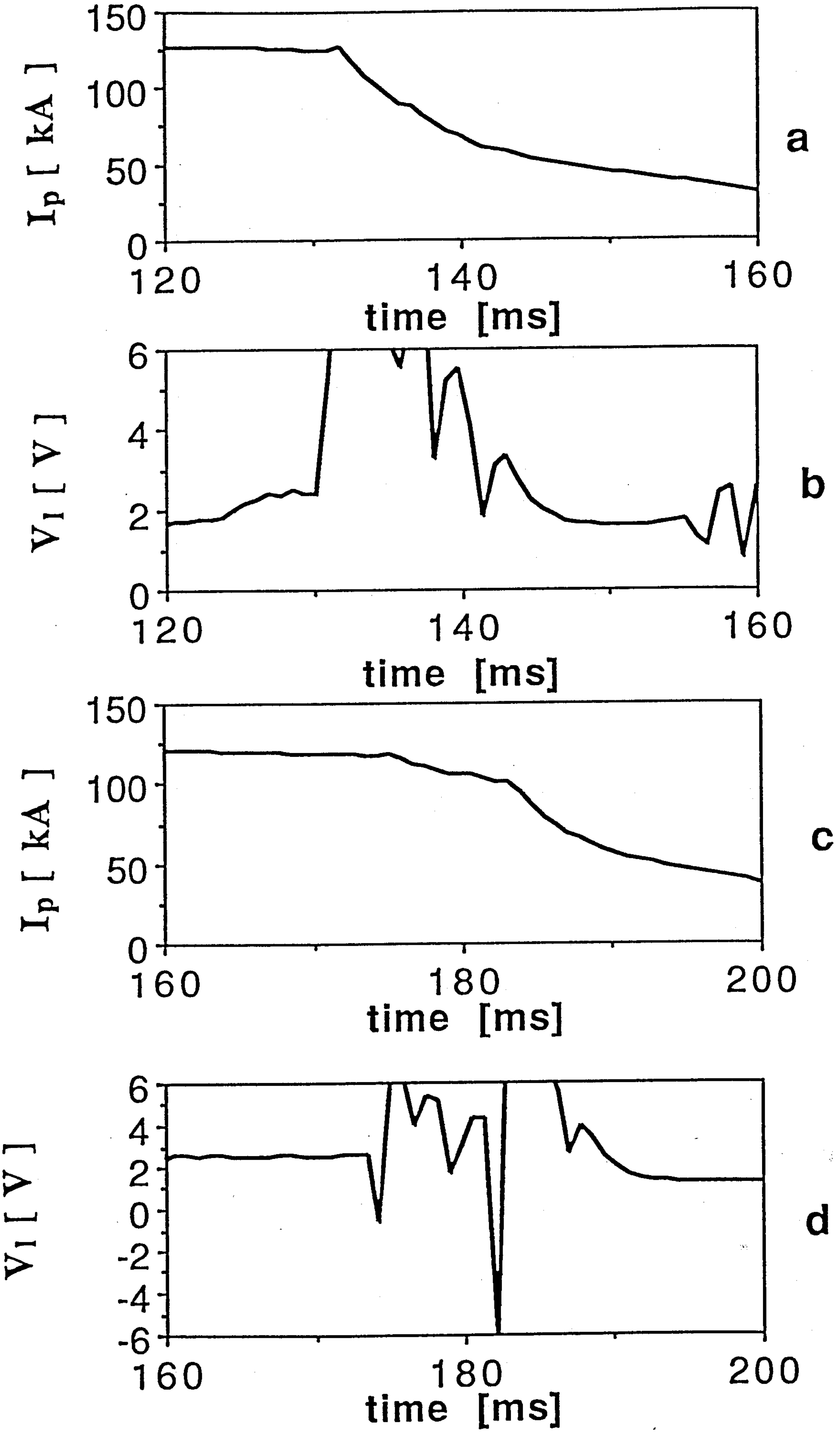
I_p [kA]
150
100
50
0
120
140
160
time [ms]
a
V_l [V]
6
4
2
0
120
140
160
time [ms]
b
I_p [kA]
150
100
50
0
160
180
200
time [ms]
c
V_l [V]
6
4
2
0
-2
-4
-6
160
180
200
time [ms]
d

Figure 19

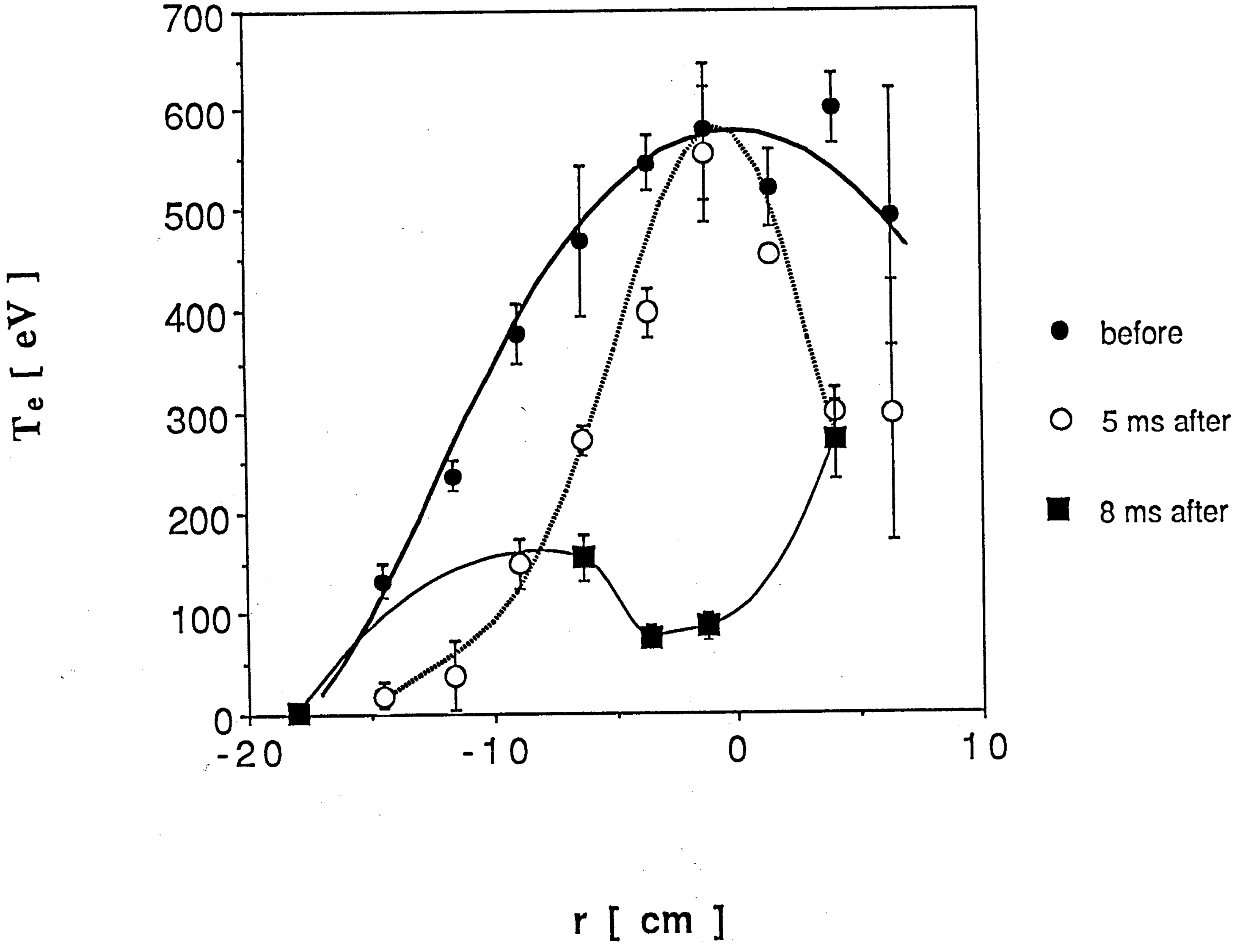
T_e [eV]
700
600
500
400
300
200
100
0
-20
-10
0
10
r [cm]
● before
○ 5 ms after
■ 8 ms after

Figure 20

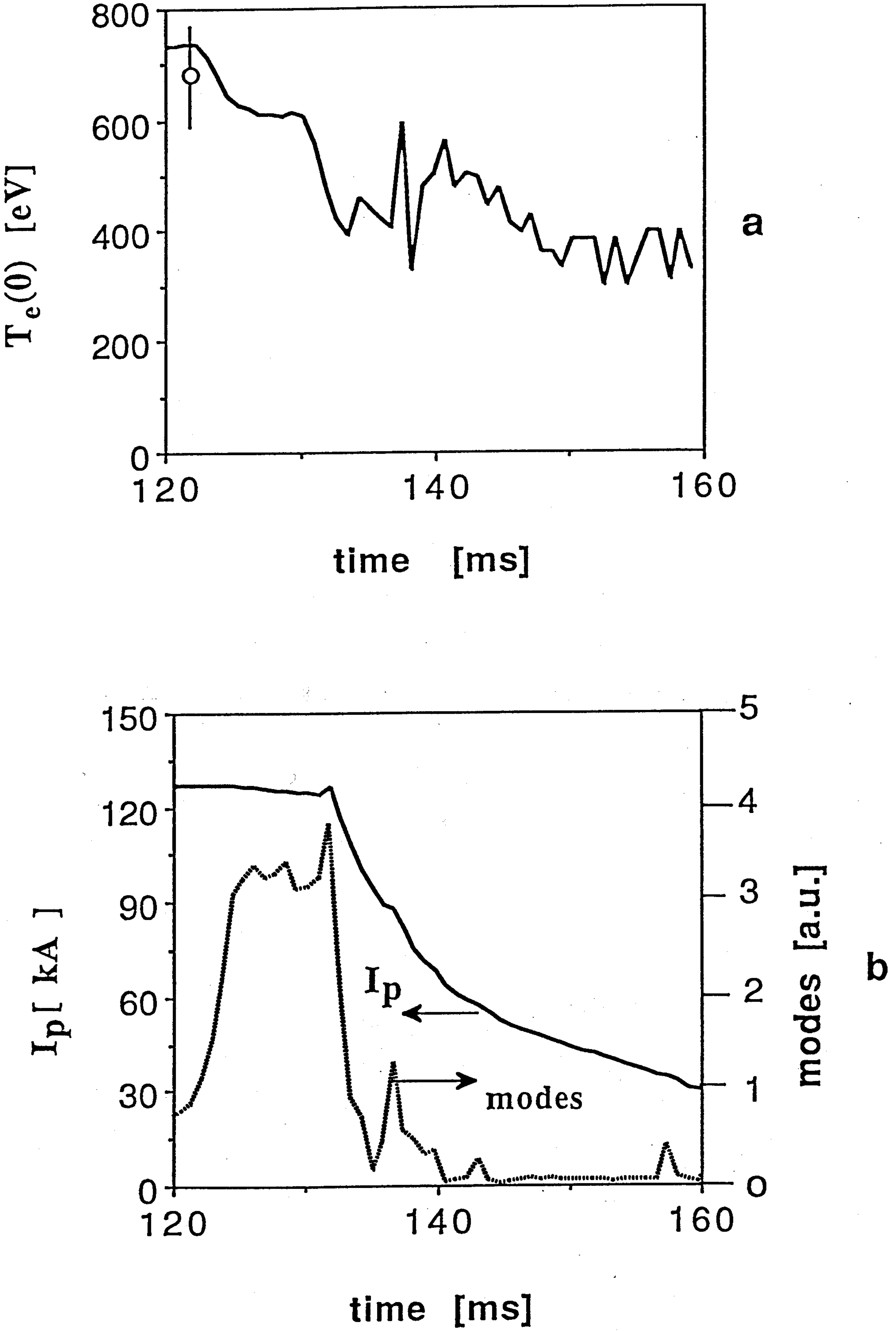
800
600
400
200
0
$T_e(0)$ [eV]
120
140
160
time [ms]
a
150
120
90
60
30
0
I_p[kA]
5
4
3
2
1
0
modes [a.u.]
I_p
modes
120
140
160
time [ms]
b

Figure 21

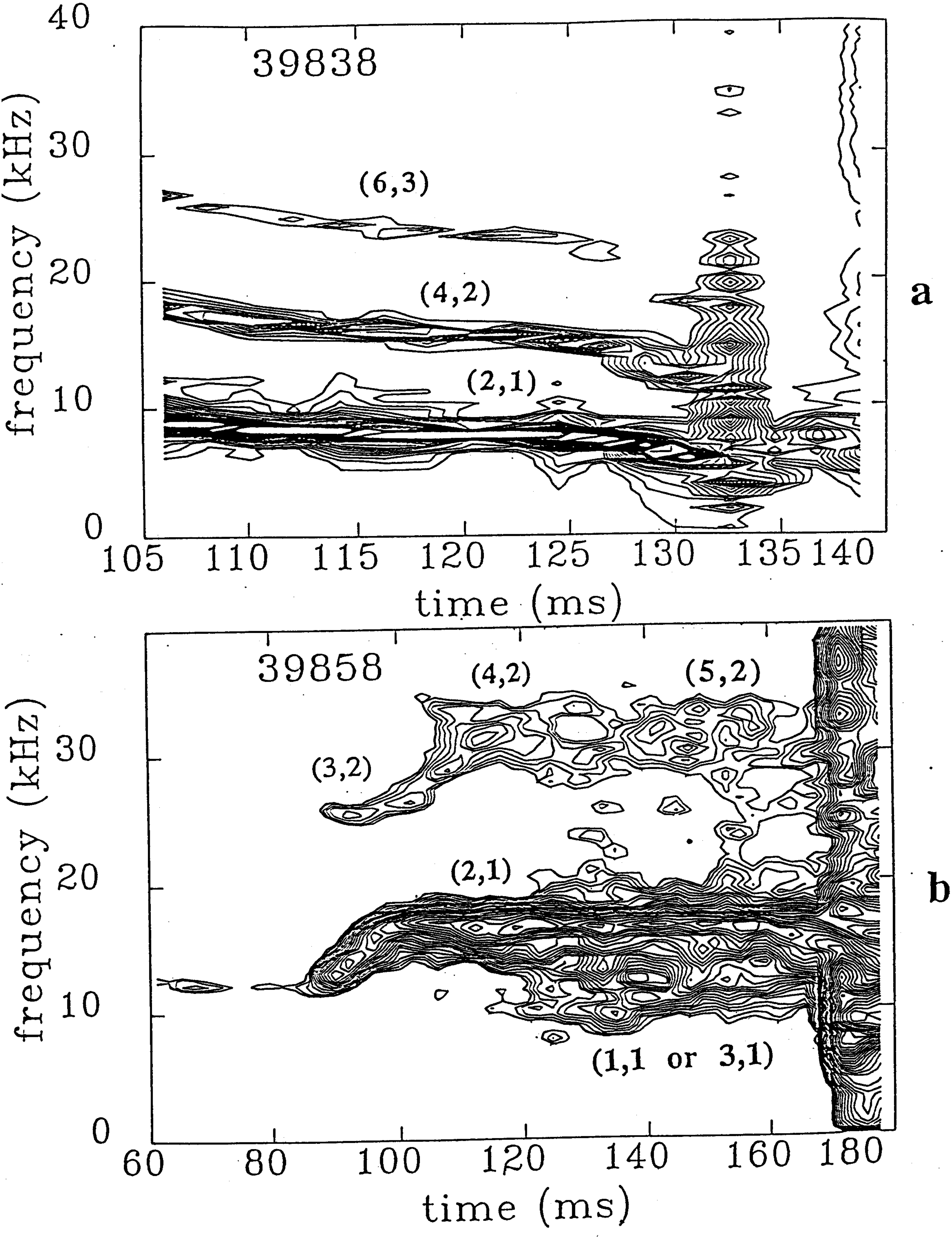
39838
(6,3)
(4,2)
(2,1)
a
frequency (kHz)
0
10
20
30
40
105
110
115
120
125
130
135
140
time (ms)
39858
(4,2)
(5,2)
(3,2)
(2,1)
(1,1 or 3,1)
b
frequency (kHz)
0
10
20
30
60
80
100
120
140
160
180
time (ms)

Figure 22

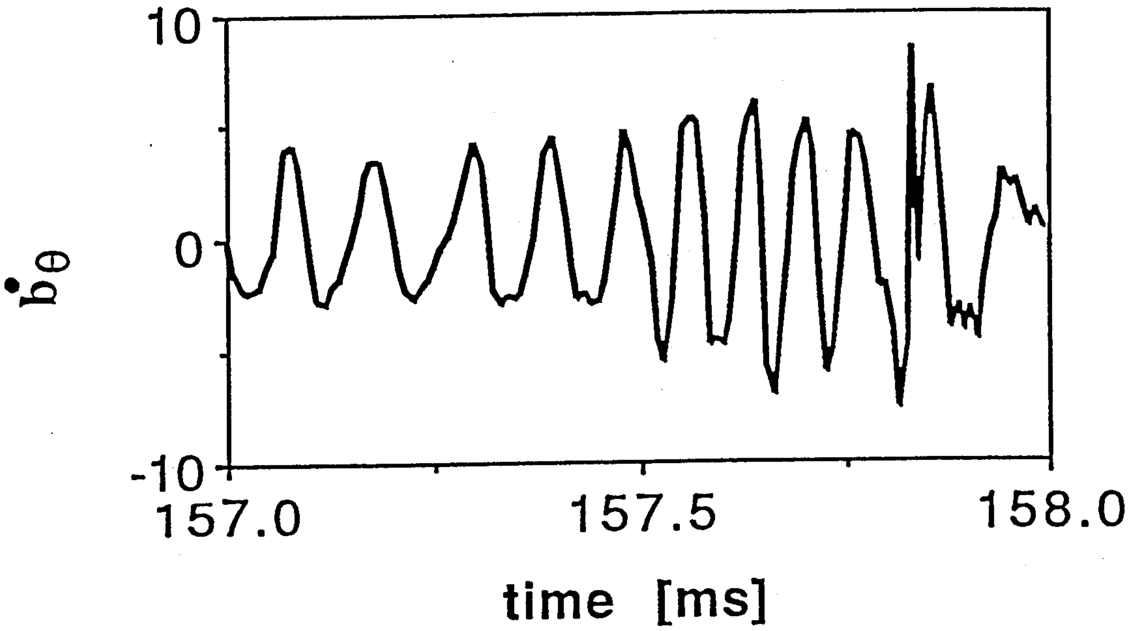

Figure 23

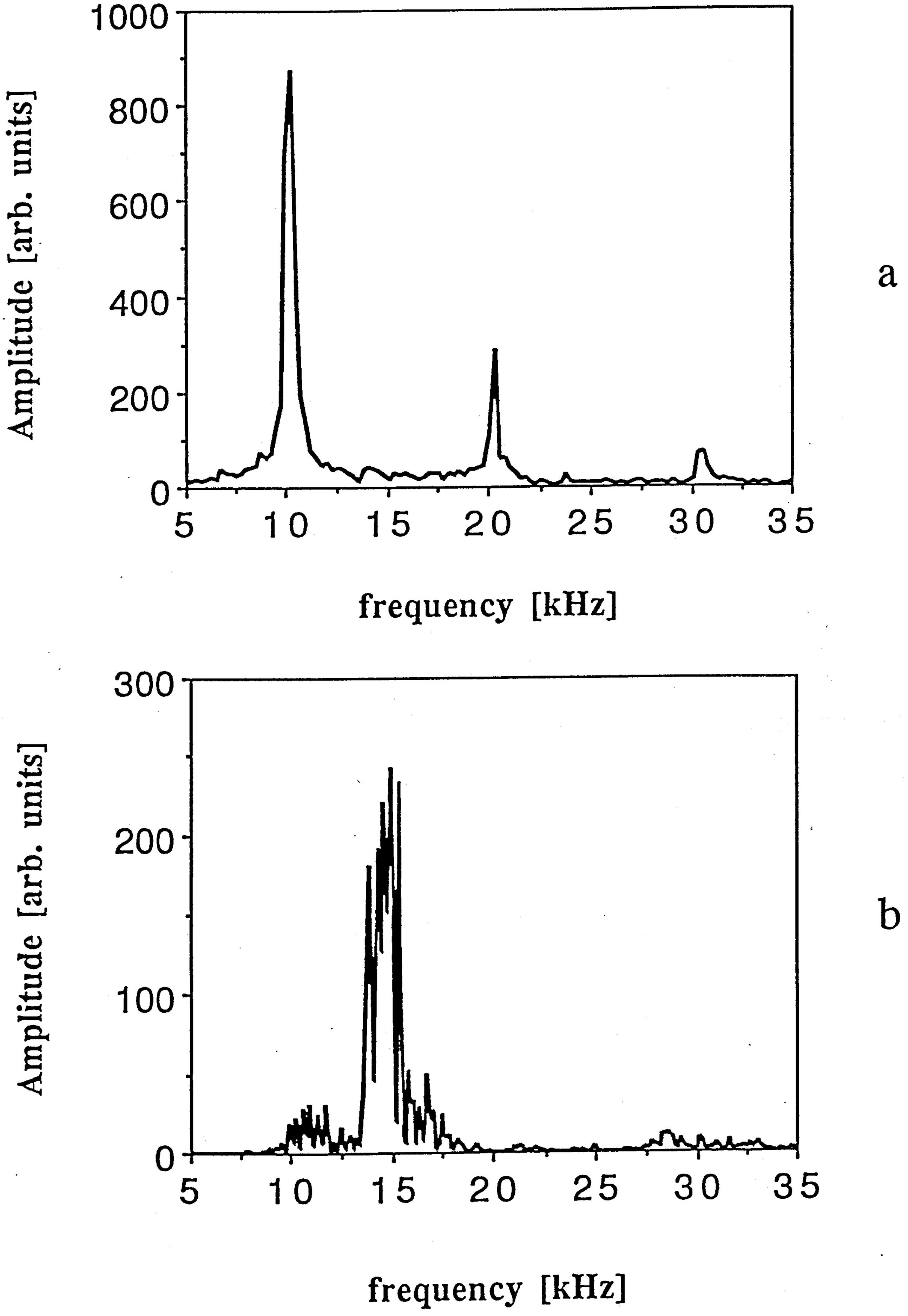
Amplitude [arb. units]
1000
800
600
400
200
0
5
10
15
20
25
30
35
frequency [kHz]
a
Amplitude [arb. units]
300
200
100
0
5
10
15
20
25
30
35
frequency [kHz]
b

Figure 24

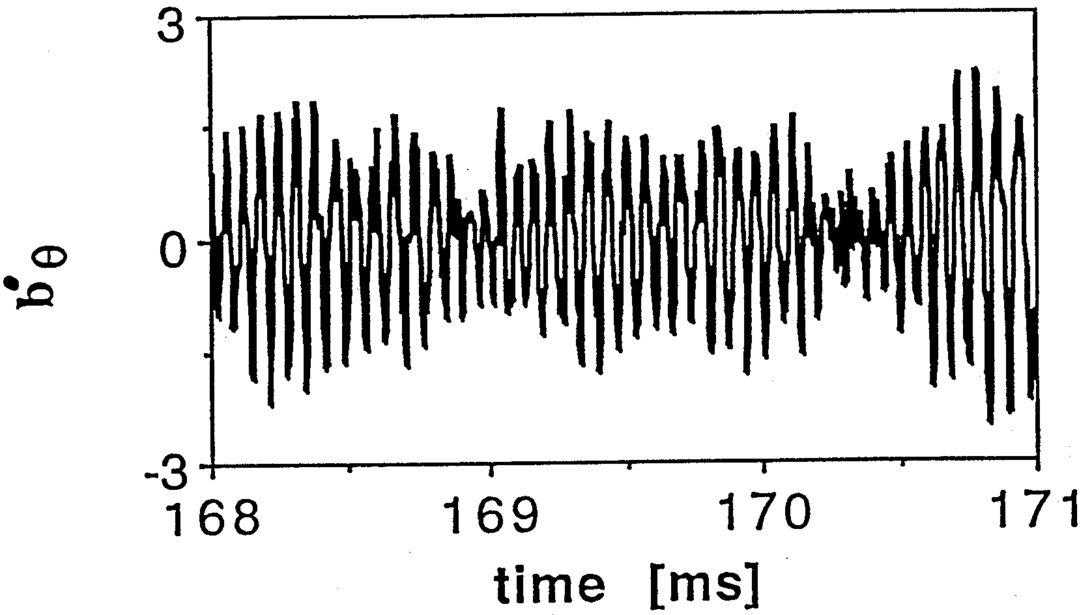

Figure 25

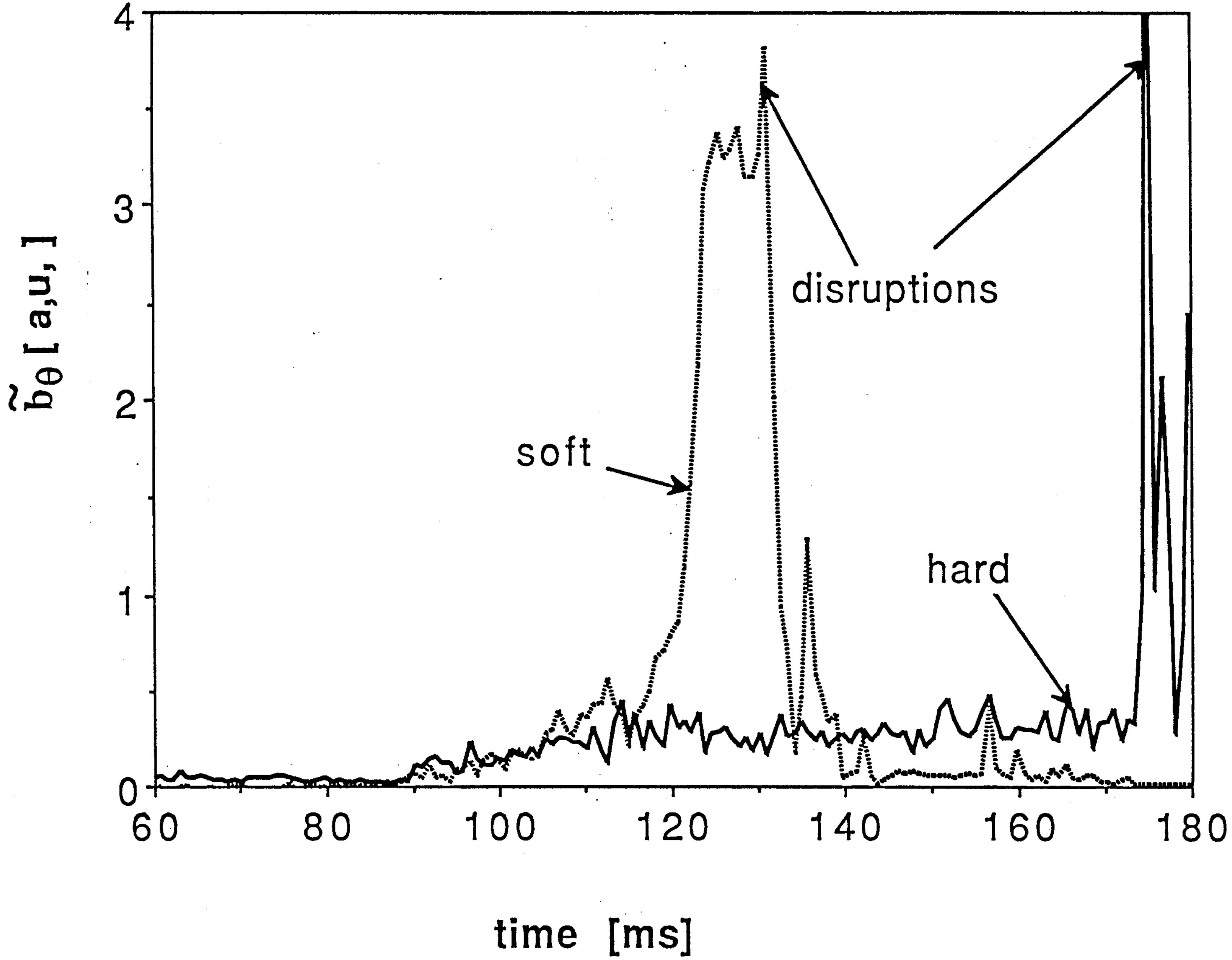

$\tilde{b}_\theta$ [a,u,]
4
3
2
1
0
60
80
100
120
140
160
180
time [ms]
disruptions
soft
hard

Figure 26

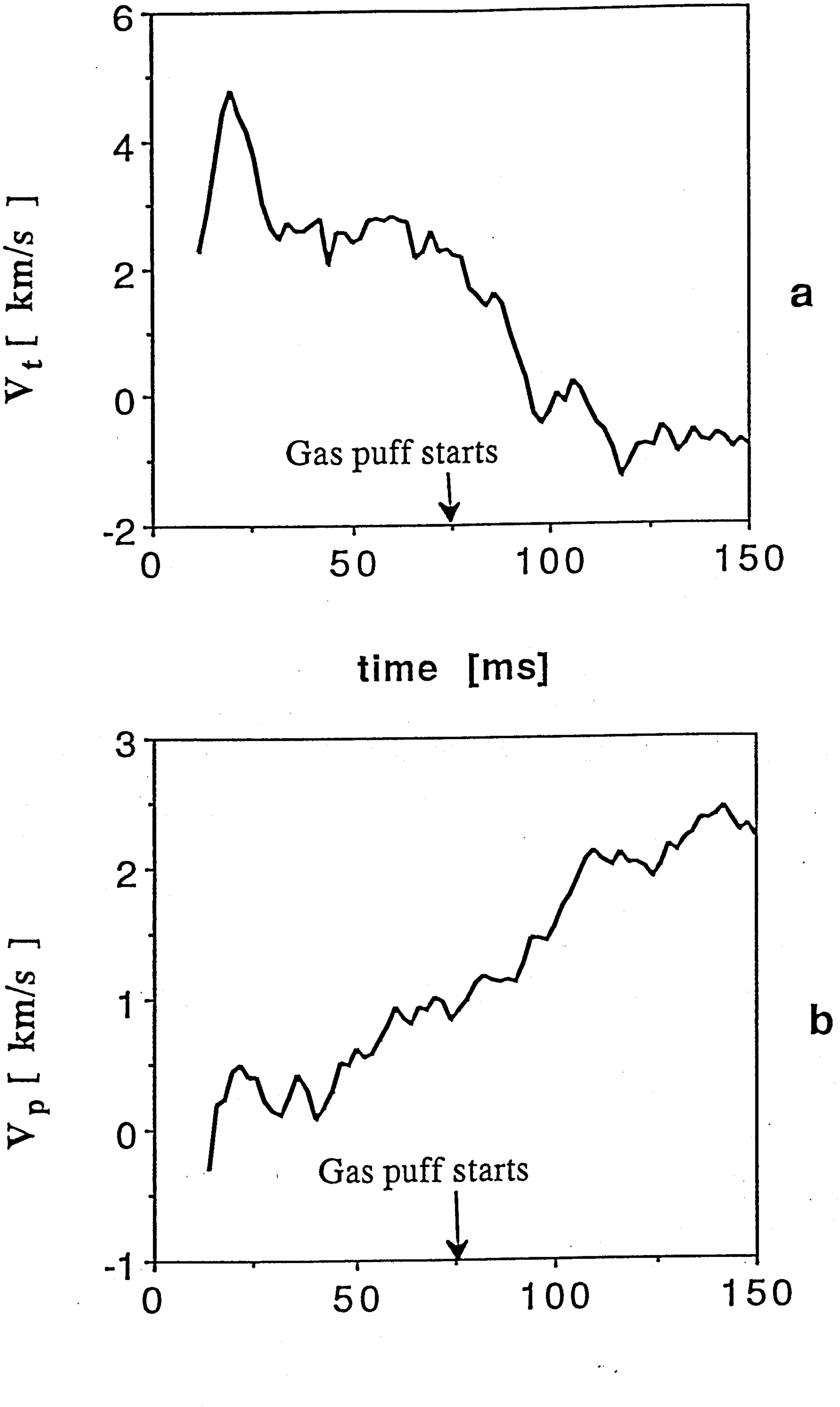
6
4
2
0
-2
0
50
100
150
V$_t$ [km/s]
time [ms]
Gas puff starts
a
3
2
1
0
-1
0
50
100
150
V$_p$ [km/s]
time [ms]
Gas puff starts
b

Figure 27

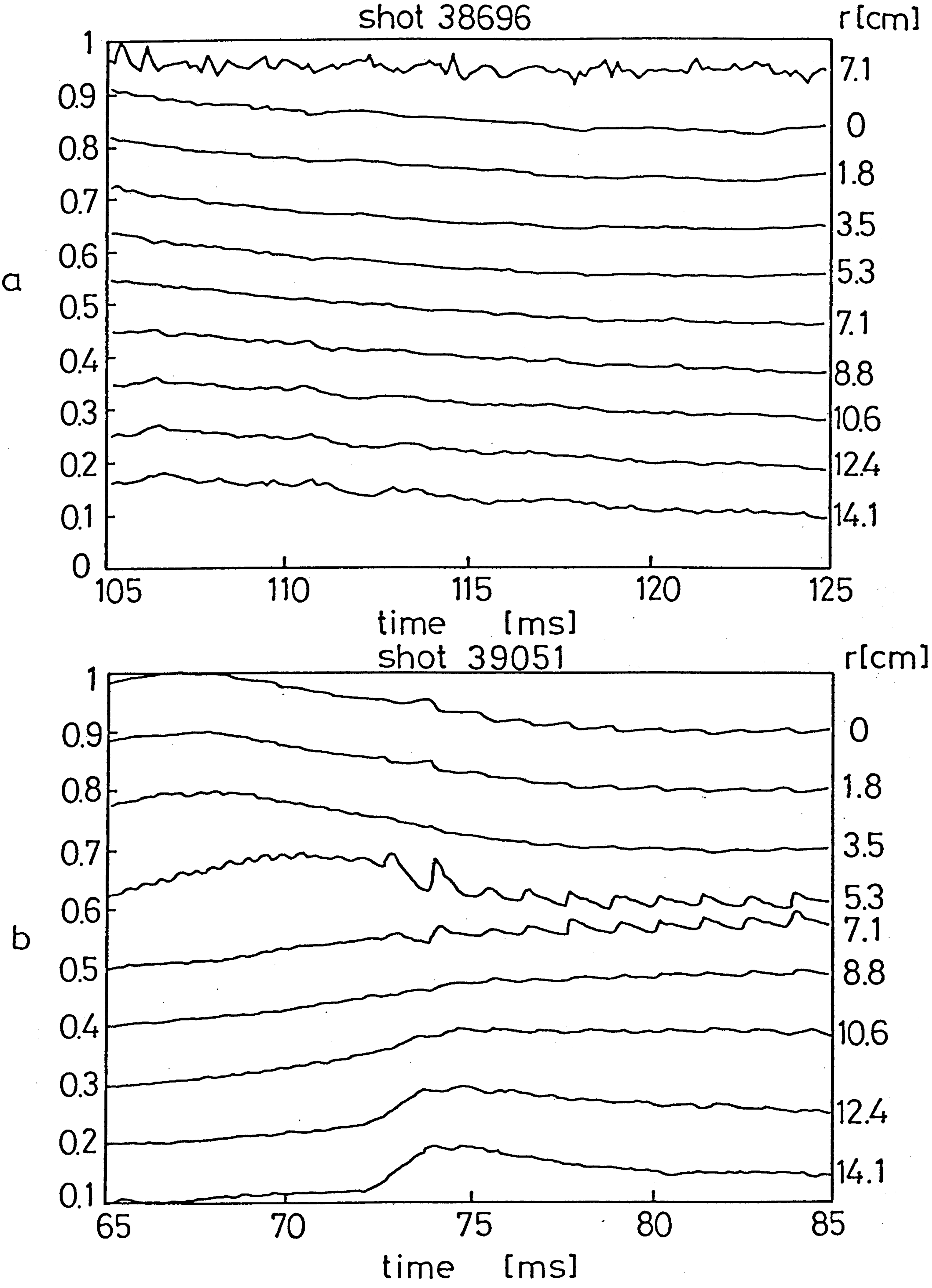
a
shot 38696
r[cm]
7.1
0
1.8
3.5
5.3
7.1
8.8
10.6
12.4
14.1
1
0.9
0.8
0.7
0.6
0.5
0.4
0.3
0.2
0.1
0
105
110
115
120
125
time [ms]
b
shot 39051
r[cm]
0
1.8
3.5
5.3
7.1
8.8
10.6
12.4
14.1
1
0.9
0.8
0.7
0.6
0.5
0.4
0.3
0.2
0.1
65
70
75
80
85
time [ms]

Figure 28

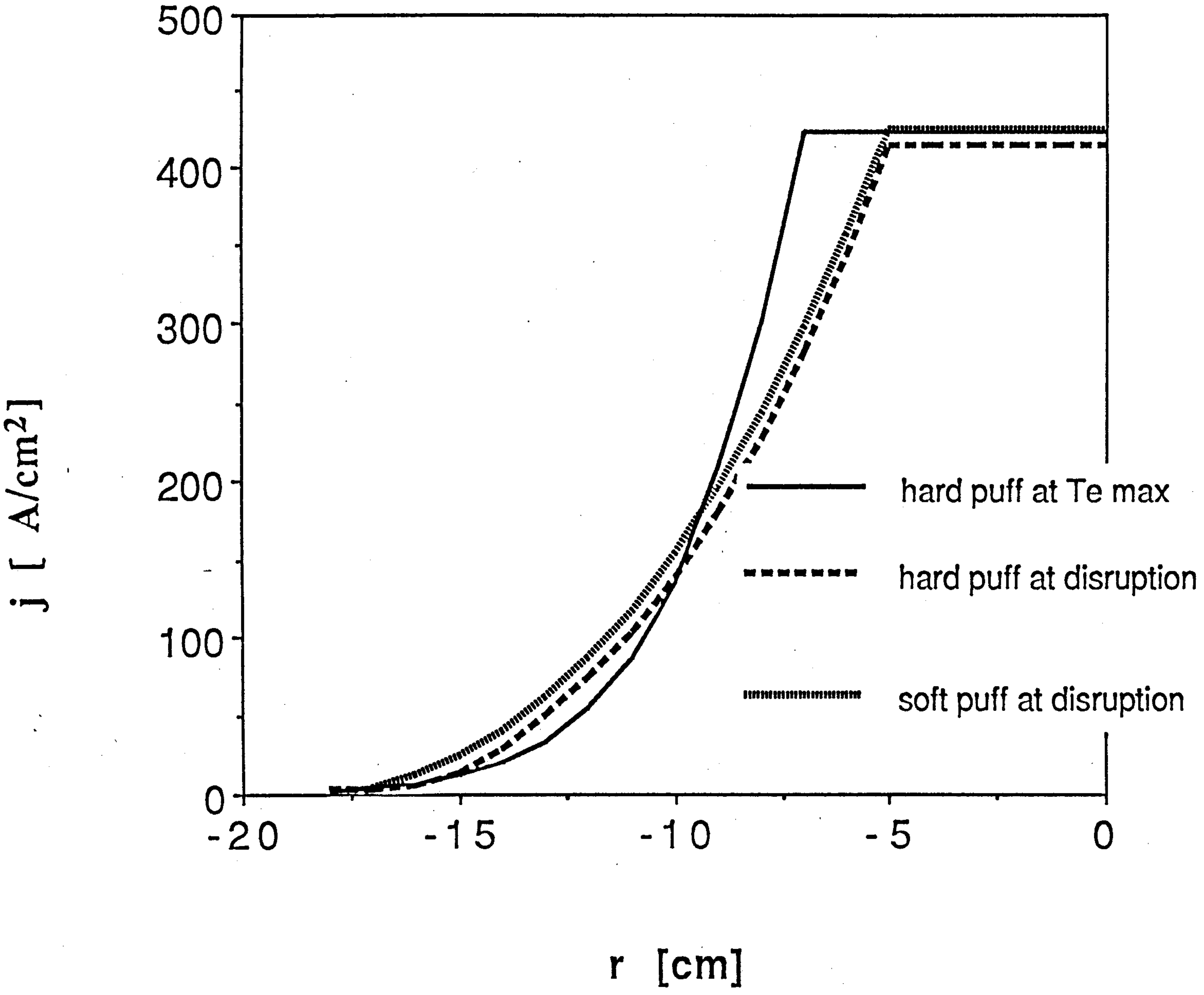
500
400
300
200
100
0
j [A/cm²]
-20
-15
-10
-5
0
r [cm]
hard puff at Te max
hard puff at disruption
soft puff at disruption

Figure 29

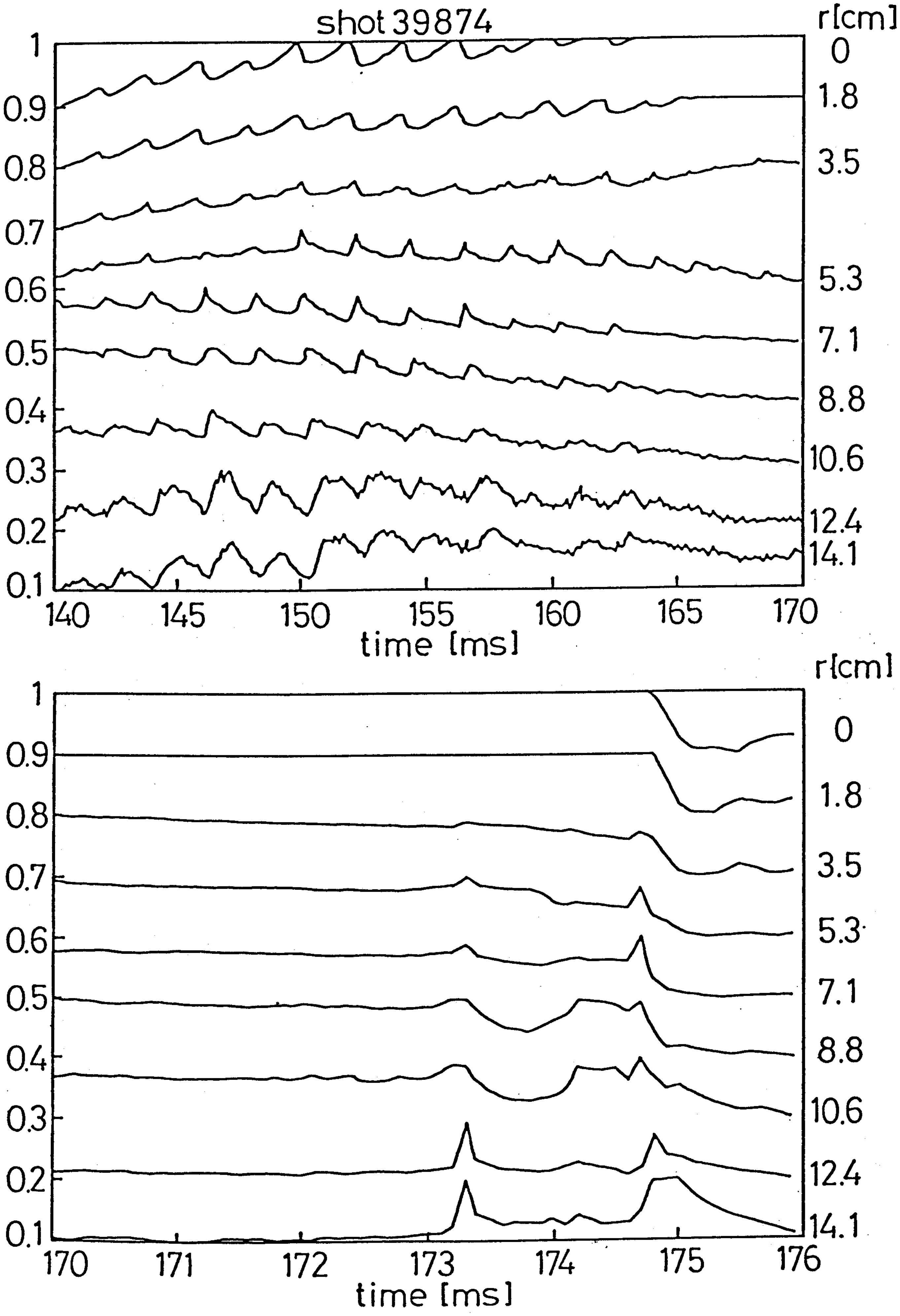
shot 39874
r[cm]
0
1.8
3.5
5.3
7.1
8.8
10.6
12.4
14.1
1
0.9
0.8
0.7
0.6
0.5
0.4
0.3
0.2
0.1
140
145
150
155
160
165
170
time [ms]
r[cm]
0
1.8
3.5
5.3
7.1
8.8
10.6
12.4
14.1
1
0.9
0.8
0.7
0.6
0.5
0.4
0.3
0.2
0.1
170
171
172
173
174
175
176
time [ms]

Figure 30

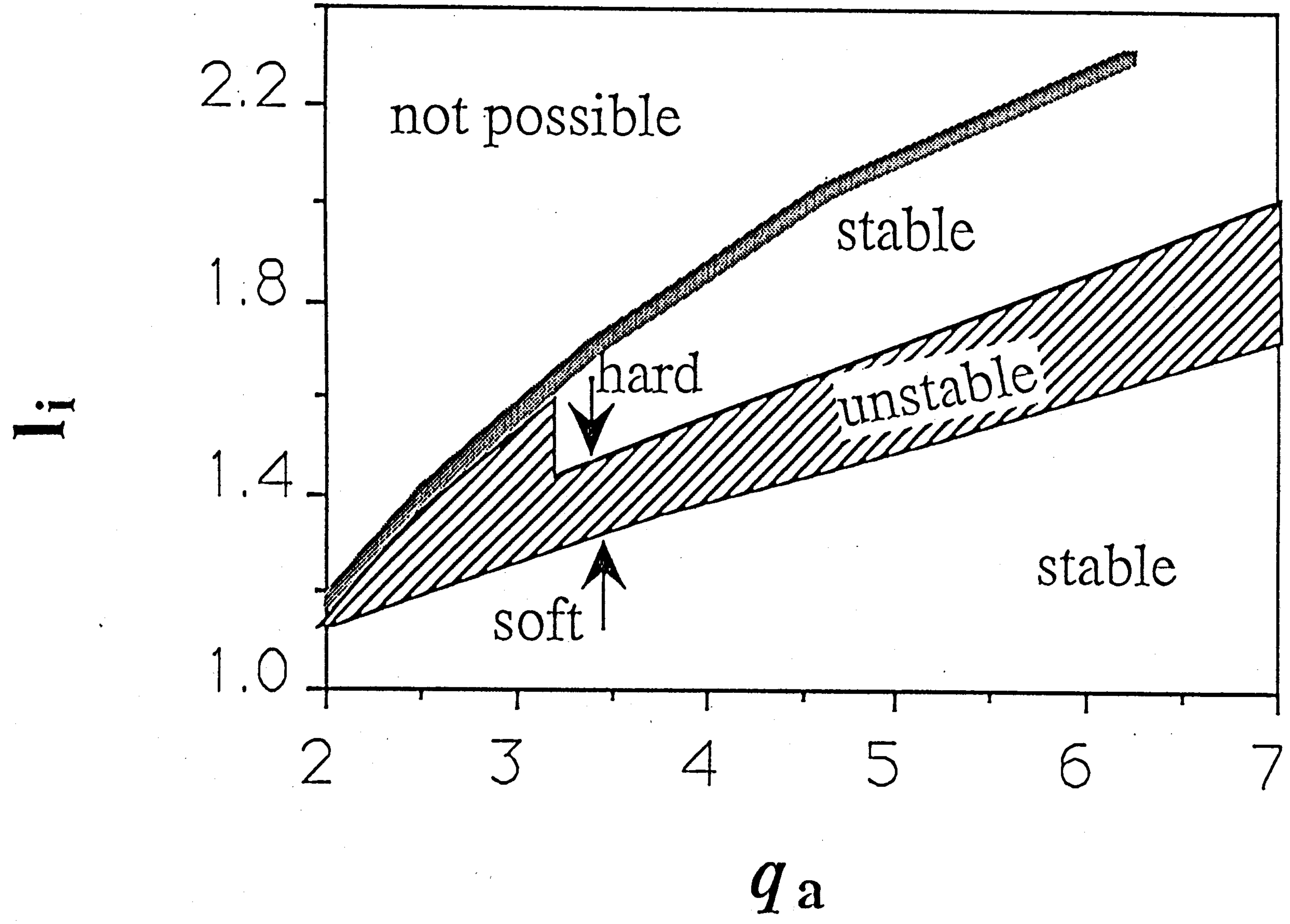
not possible
stable
hard
unstable
soft
stable
2.2
1.8
1.4
1.0
l_i
2
3
4
5
6
7
q_a

Figure 31

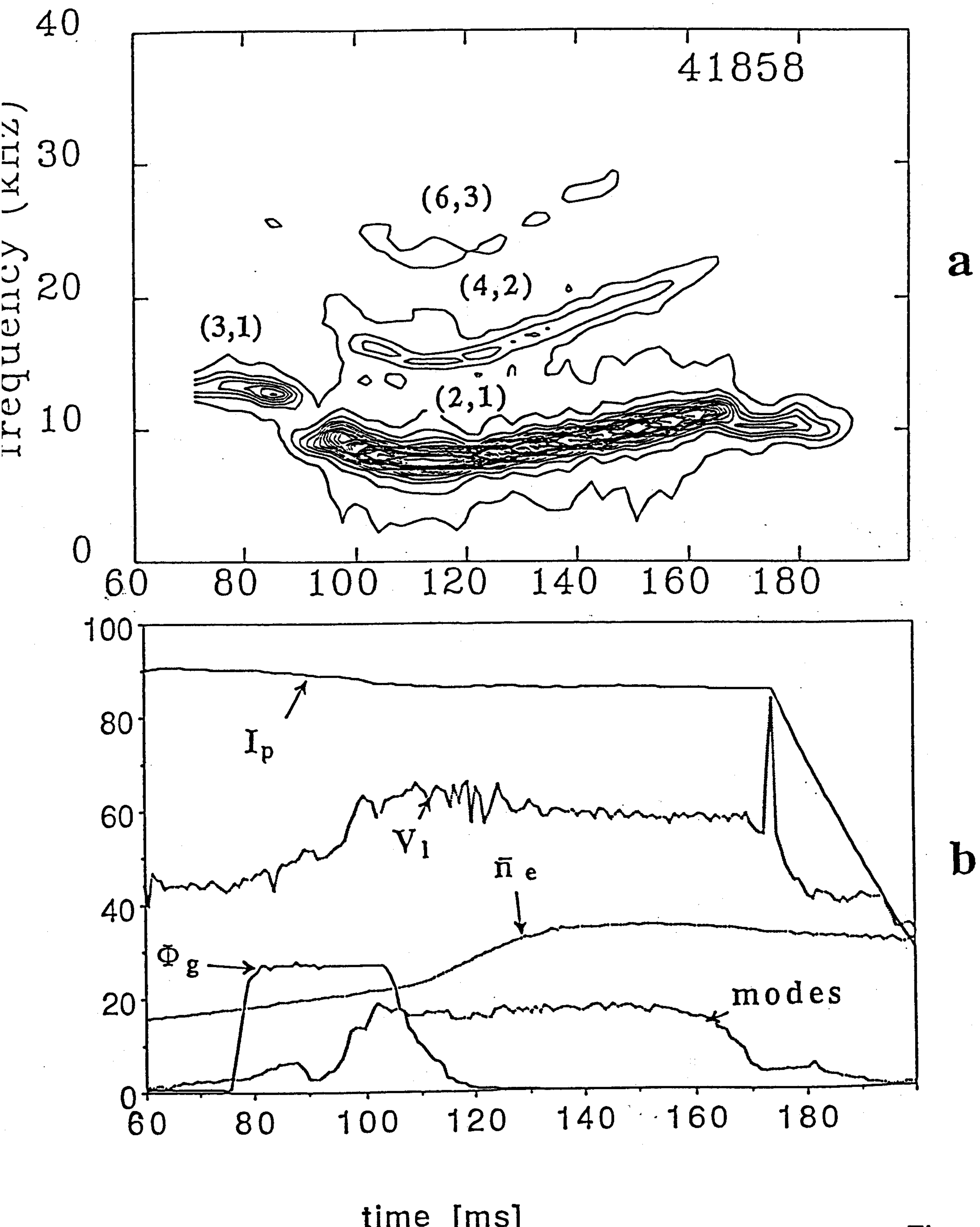

41858
(6,3)
(4,2)
(3,1)
(2,1)
frequency (kHz)
40
30
20
10
0
60
80
100
120
140
160
180
a
100
80
60
40
20
0
I_p
V_l
n̄ e
Φ g
modes
b
time [ms]

Figure 32